A numerical model for design and optimization of surface textures for tilting pad thrust bearings

Daniel Gropper [*], Terry J. Harvey, Ling Wang

National Centre for Advanced Tribology at Southampton (nCATS), Faculty of Engineering and the Environment, University of Southampton, Southampton SO17 1BJ, UK

ABSTRACT

A numerical model based on the Reynolds equation to study textured tilting pad thrust bearings considering mass-conserving cavitation and thermal effects is presented. A non-uniform and adaptive finite volume method is utilized and two methods are compared and selected regarding their efficiency in handling discontinuities; specifically placing additional nodes closely around discontinuities and directly incorporating discontinuities in the discrete system. Multithreading is applied to improve the computational performance and three root-finding methods to evaluate the bearing equilibrium are compared; namely Newton-Raphson method, Broyden's method with Sherman-Morrison formula and a continuation approach with fourth-order Runge-Kutta method. Results from the equivalent untextured bearing are utilized to accelerate the computation of the textured bearing and results are validated by comparison with CFD data.

1. Introduction

Surface texturing is becoming a promising method for enhancing the performance of hydrodynamic bearings in terms of increasing the oil film thickness and reducing the frictional loss for a safer and more efficient bearing operation. However, successful industrial applications of textured bearings are still limited. One of the main challenges is the dependency of optimum texturing parameters on the type of contact and the operating conditions [1]. A poor texture selection may even lead to a deterioration of the bearing performance. This makes the design of optimized texture patterns a challenging task, which generally requires the utilization of advanced computational models due to the large number of parameters involved. Hence, a successful application of surface texturing relies to a great degree on fast and robust mathematical models that allow an accurate evaluation of the impact of surface textures on the performance of bearings under a wide range of conditions.

The key task in the theoretical analysis of hydrodynamic bearings is the solution of the Reynolds equation to obtain the pressure field, which after integration yields the bearing's main performance parameters, such as load carrying capacity, friction and power loss. While solving the Reynolds equation is quite straightforward for conventional bearings, a number of issues are encountered when simulating textured bearings. For example, texturing can result in the development of multiple cavitation zones and consequently a mass-conserving mathematical treatment of

cavitation becomes necessary [2,3]. Also, the fine meshes generally required to capture the complex geometry of textured bearings result in significantly increased computation times. Furthermore, textures introduce numerous discontinuities in the film thickness distribution, which if untreated, can lead to considerable discretization errors. One of the most popular discretization methods in the field of hydrodynamic lubrication is the finite volume method (FVM) due to its simplicity and mass-conserving properties. Unlike methods based on the weak solution of the Reynolds equation, e.g. finite element methods, the FVM is based on boundary flux approximations, i.e. derivatives at film discontinuities directly depend on the mesh size. Consequently, discontinuities should be treated in order to avoid large discretization errors or high computation times caused by fine meshes. Two ways to deal with discontinuities in finite difference based approaches are available: A local mesh refinement [4,5] and a direct incorporation of discontinuities in the discrete system as proposed by Arghir et al. in 2002 [6]. However, these methods have not been evaluated previously regarding their capability of decreasing discretization errors or reducing computation times. Despite the benefits, discontinuities are rarely directly handled in finite difference based numerical approaches, resulting in unnecessarily fine meshes and high computation times.

Another key step in the analysis of hydrodynamic bearings is the evaluation of the bearing equilibrium, i.e. the specific film geometry that balances the applied load. This generally requires solving the Reynolds

---

Nomenclature

a	coefficient for the discrete system (m.s or kg/s)
a	coefficient for viscosity temperature relationship
A	control volume face dimension (m or rad)
B	interface Bernoulli coefficient (Pa)
B_P	Bernoulli coefficient (kg/s)
b	coefficient for the discrete system (m.s)
c_p	lubricant specific heat (J/kg/K)
D	damping parameter
d_f	discontinuity coefficient
e_p, e_e, e_t	tolerance value for pressure, equilibrium and temperature solver
$\boldsymbol{F}$	nonlinear system for equilibrium solver
f	interpolation factor
$\boldsymbol{G}$	homotopy function
h	local film thickness (m)
h_p	film thickness at pivot (m)
$h_{texture}$	texture depth (m)
ii	total number of nodes in radial direction
$\boldsymbol{J}$	Jacobian matrix
J_P	jump coefficient (kg/s)
jj	total number of nodes in circumferential direction
k_{con}	convection parameter
m, n	coefficients for viscosity temperature relationship
n_{pad}	number of pads
n_r	number of textures in radial direction
n_θ	number of textures in circumferential direction
p	local pressure (Pa)
p_{cav}	cavitation pressure (Pa)
Q	volumetric flow rate (m³/s)
q	mass flow rate (kg/s)
r	radial coordinate (m)
r_i	inner pad radius (m)
r_o	outer pad radius (m)
r_p	radial coordinate of pivot (m)
T	temperature (°C)
T_f	friction torque (Nm)
$T_{°K}$	temperature (°K)
u	average fluid velocity (m/s)
w_0	applied specific load (MPa)
$\boldsymbol{x}$	solution vector for equilibrium solver
x, y	Cartesian coordinates (m)
α	relative texture extend in circumferential direction

α_r, α_θ	pitch and roll angle (rad)
β	relative texture extend in radial direction
Γ	diffusion coefficient (m.s)
δr	radial distance from centre of pressure to pivot (m)
δW	difference in load carrying capacity and applied load (N)
$\delta\theta$	circumferential distance from centre of pressure to pivot (rad)
$\varepsilon_p, \varepsilon_e, \varepsilon_t$	fractional residuals for pressure, equilibrium and temperature solver
η	lubricant dynamic viscosity (Pa.s)
Θ	fractional film content
θ	circumferential coordinate (rad)
θ_p	circumferential coordinate of pivot (rad)
θ_{pad}	pad angle (°)
λ	homotopy parameter
ν_{40}, ν_{100}	lubricant kinematic viscosity at 40 °C and 100 °C (cSt)
ν_{cSt}	lubricant kinematic viscosity (cSt)
ξ	pressure drop coefficient
Π	frictional power loss (W)
ρ	lubricant density (kg/m³)
ρ_r	texture density in radial direction
ρ_θ	texture density in circumferential direction
ω	rotational speed (1/s)
ω_p, ω_Θ	relaxation parameter for pressure and fractional film content
$\mathscr{D}^+$	pressurized regions
$\mathscr{D}^0$	cavitated regions
$\mathscr{F}$	computational domain

Subscripts and superscripts

$-, +$	value just before and after discontinuity
eff	effective quantity
i, j	control volume indices
ir	quantity at pad inner radius
k	iteration number
max	maximum
min	minimum
opt	optimum
out	quantity at pad outlet
sup	supplied quantity
W, E, S, N, P	west, east, south, north, central nodal value
w, e, s, n	west, east, south, north boundary value

equation multiple times for different film geometries. Due to the increased complexity in solving the Reynolds equation for textured bearings, effective methods for finding the bearing equilibrium are crucial. While numerous root-finding methods to evaluate the bearing equilibrium are available, the majority of numerical studies are based on the Newton-Raphson method due to its simplicity and quadratic convergence. However, this method requires the determination of the Jacobian matrix at each iteration and an initial film thickness guess sufficiently close to the actual solution in order to converge. Other methods, such as Broyden's method or continuation methods may provide enhanced stability and computational performance when applied instead of the Newton-Raphson method or in combination with the Newton-Raphson method.

The aim of this work was the development of a fast and robust numerical model to analyse the influence of surface texturing on the performance of tilting pad thrust bearings. To allow for parametric studies and the optimization of texture designs, the model is optimized in terms of computational speed and robustness. The model is based on a finite volume discretization of the Reynolds equation while considering mass-conserving cavitation and thermal effects. Two methods of handling discontinuities (local mesh refinement and the direct incorporation in the discrete system) and three different root-finding methods (Newton-Raphson method, Broyden's method and a continuation method) are compared and selected based on computation speed and numerical stability. Computation times are decreased by utilizing results from the equivalent untextured bearing and results are validated through comparison with data from commercial CFD published in literature.

2. The model

2.1. Bearing geometry and film thickness

A point-pivoted tilting pad thrust bearing and details of its pads are shown in Fig. 1.

Under the assumption that bearing and runner are perfectly aligned, it is sufficient to model only one of the pads and subsequently extrapolate the results to obtain the overall bearing performance. Each pad is supported by a point pivot, allowing them to tilt freely about a certain radial line, given by the pitch angle α_r, and a certain tangential line, given by the roll angle α_θ. During operation, each pad will self-adjust its tilt angles to realize a film geometry that balances the encountered operating conditions. Using a polar coordinate system, the local film thickness at each point on the pad can be expressed as:

$$h(\theta, r) = h_p + r \sin(\theta_p - \theta) \sin \alpha_r + \left[r_p - r \cos(\theta_p - \theta) \right] \sin \alpha_\theta \qquad (1)$$

where h_p is the film thickness at the pivot and θ_p, r_p are the coordinates of the pivot. The considered operating conditions result in purely hydrodynamic lubrication with large lambda ratios and therefore surface roughness is not considered.

In the present model, each texture pattern is defined by the number of textures in circumferential and radial direction (n_θ and n_r), the relative texture extend in circumferential and radial direction (α and β), the texture density in circumferential and radial direction (ρ_θ and ρ_r) and the texture depth $h_{texture}$. This methodology ensures a simple generation of a variety of texture designs, including fully textured, partially textured, grooved and pocketed pads (see Fig. 2). To texture the inlet, the first texture row is simply elongated towards the inlet. Only partially textured pads and angular sector shaped textures with flat bottom profile are considered, as this type of texture pattern most closely reassembles a stepped configuration, which has been shown to have the most beneficial impact on the bearing performance [7,8].

2.2. Fluid mechanics

The present model is based on the steady-state Reynolds equation for incompressible fluids. Cavitation does not usually occur in textured tilting pad thrust bearings as the overall convergence builds up enough pressure to prevent pressures from falling below the cavitation pressure. However, under operating conditions that result in particularly low convergence ratios or whenever deep textures are analysed, cavitation

Fig. 1. Bearing geometry and film thickness: (a) Pad details with coordinate system and (b) tilting pad thrust bearing geometry.

may occur inside individual textures close to the pad inlet at the outer pad radius. Therefore, a mass-conserving form of the Reynolds equation is used, where the well-known Jakobsson-Floberg-Olsson (JFO) boundary conditions are incorporated [9,10]. Based on the approaches by Ausas [2] and Bartel [11], the applied modified Reynolds equation reads:

$$\frac{\partial}{\partial r}\left(r \frac{\rho h^3}{\eta} \frac{\partial p}{\partial r} \right) + \frac{1}{r} \frac{\partial}{\partial \theta}\left(\frac{\rho h^3}{\eta} \frac{\partial p}{\partial \theta} \right) = 6\omega r \frac{\partial(\Theta \rho h)}{\partial \theta} \qquad (2)$$

where p is the local pressure, ρ the lubricant density, η the lubricant dynamic viscosity and Θ the fractional film content, which is defined as:

$$\Theta = 1 \text{ and } p > p_{cav} \text{ in pressurized region } \left(\mathscr{D}^+ \right) \qquad (3)$$

$$\Theta < 1 \text{ and } p = p_{cav} \text{ in cavitated regions } \left(\mathscr{D}^0 \right) \qquad (4)$$

where p_{cav} is the cavitation pressure. Here, $p_{cav} = 10^{-6}$ Pa rather than 0 Pa to avoid numerical instability. Equation (2) is valid over the entire solution domain ($\mathscr{F}$) and can be solved for pressure and fractional film content simultaneously.

2.3. Discretization

A FVM is used to discretize the modified Reynolds equation, since for textured bearings this method has been shown to be a good compromise between accuracy and implementation complexity [12,13]. The computational domain is divided into a number of discrete control volumes (CVs) while a node is placed at the centre of each CV [14] (see Fig. 3).

For textured pads, a non-uniform mesh is applied instead of a uniform mesh for the following reasons.

- A fine mesh can be used for textured pad areas, where the complex texture geometry requires a fine mesh, and a coarse mesh for untextured areas, where a coarse mesh is sufficient to describe the simple, smooth geometry resulting in a more efficient solution of the Reynolds equation.
- CV faces can be aligned with film thickness discontinuities to minimize discretization errors [6].
- Additional nodes can easily be placed around discontinuities to decrease discretization errors.

Three different methods of discretization are considered and compared in this study: A conventional non-uniform finite volume discretization (NUFVD), a version of the NUFVD method where additional nodes are placed around discontinuities (NUFVD+A) and a modified NUFVD method, where discontinuities are directly incorporated during the derivation of the discrete system (MNUFVD) [6]. Details of this three methods are given below.

2.3.1. Non-uniform finite volume discretization (NUFVD)

The finite volume formulation of the Reynolds equation is based on the conservation of mass (continuity equation). Consequently, it is possible to simply balance the flows into and out of a CV:

$$q_w - q_e + q_s - q_n = 0 \qquad (5)$$

where the flows over the cell faces are defined as:

$$q_w = -\frac{A_w}{r_w} \frac{\rho_w h_w^3}{\eta_w} \left(\frac{\partial p}{\partial \theta} \right)_w + 6\omega A_w r_w \Theta_w \rho_w h_w \qquad (6)$$

$$q_e = -\frac{A_e}{r_e} \frac{\rho_e h_e^3}{\eta_e} \left(\frac{\partial p}{\partial \theta} \right)_e + 6\omega A_e r_e \Theta_e \rho_e h_e q_e \qquad (7)$$
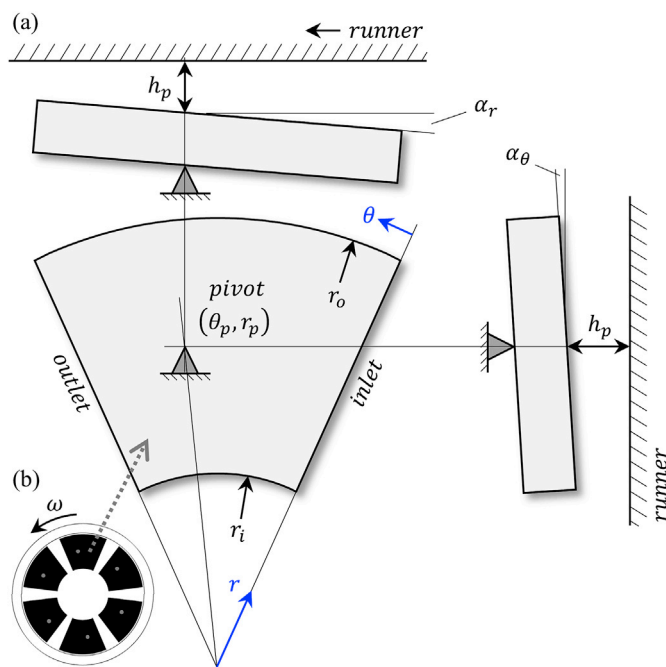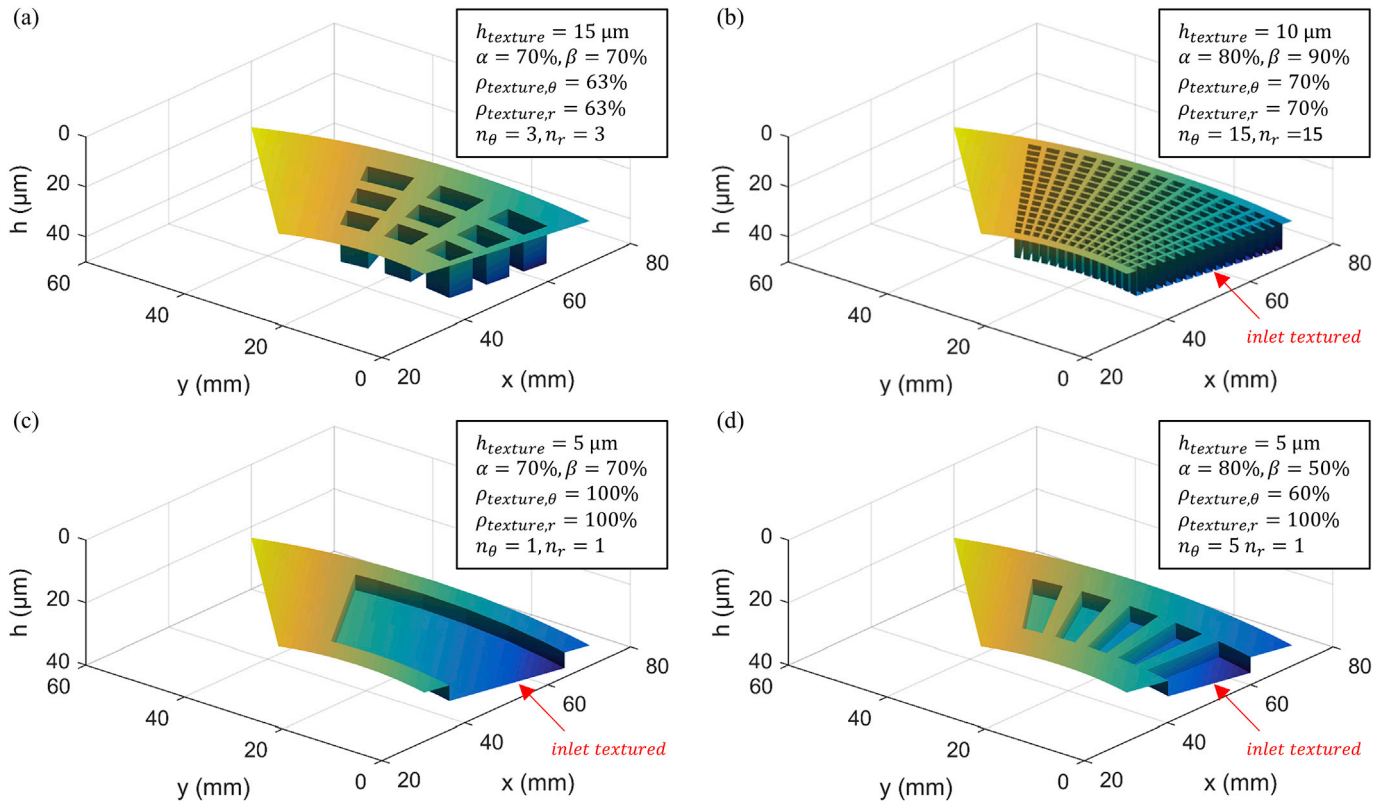
Fig. 2. Exemplary film thickness distributions for typical texture designs: (a) 3 × 3 textures, (b) 15 × 15 textures, (c) pocket and (d) 5 radial grooves.
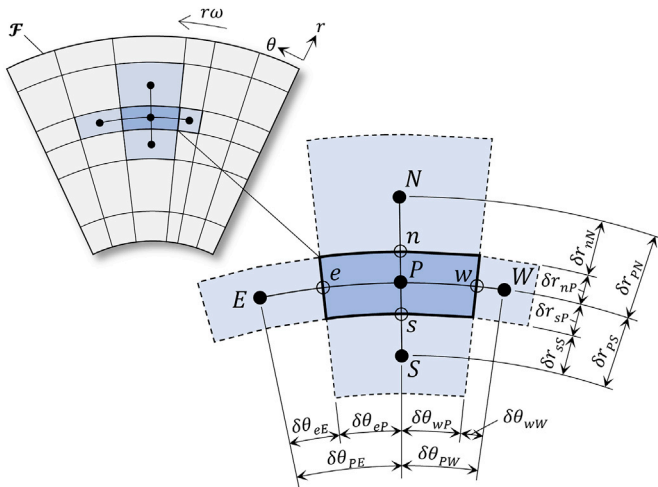

Fig. 3. Non-uniform finite volume discretization of the thrust pad with details of a control volume.

$$q_s = -A_s r_s \frac{\rho_s h_s^{\ 3}}{\eta_s} \left(\frac{\partial p}{\partial r} \right)_s \tag{8}$$

$$q_n = -A_n r_n \frac{\rho_n h_n^{\ 3}}{\eta_n} \left(\frac{\partial p}{\partial r} \right)_n \tag{9}$$

where A_w, A_e, A_s and A_n are the dimensions of the CV's west, east, south and north face respectively. The pressure gradients at the CV faces are approximated by central finite difference formulae. The second terms of equations (6) and (7) are the Couette components of the flow and are approximated by upwind schemes, hence values are simply passed along

downstream, i.e. $\Theta_w = \Theta_W$ and $\Theta_e = \Theta_P$. The interfacial diffusion coefficient at the west cell boundary is defined as:

$$\Gamma_w = \frac{\rho_w h_w^3}{\eta_w} \tag{10}$$

where h_w, ρ_w and η_w are evaluated by linear approximations according to:

$$h_w = (1 - f_w) \mathrm{h}_W + f_w \mathrm{h}_P \tag{11}$$

with the interpolation factor

$$f_w = \frac{\delta\theta_{wW}}{\delta\theta_{wW} + \delta\theta_{wP}} \tag{12}$$

Interfacial diffusion coefficients at the other cell boundaries are calculated accordingly. Finally, identifying the coefficients a_W, a_E, a_S, a_N, a_P, $a_{\Theta W}$, $a_{\Theta P}$ and rearranging, the equations for the nodal values of pressure and fractional film content are obtained:

$$p_P = \frac{1}{a_P} \left(a_E p_E + a_W p_W + a_N p_N + a_S p_S + a_{\Theta W} \Theta_W + a_{\Theta P} \Theta_P \right) \tag{13}$$

and

$$\Theta_P = -\frac{1}{a_{\Theta P}} \left(a_E p_E + a_W p_W + a_N p_N + a_S p_S - a_P p_P + a_{\Theta W} \Theta_W \right) \tag{14}$$

Formulating these equations for every internal node results in a linear algebraic system, which can be solved with appropriate boundary conditions. A full list of the coefficients used is given in Appendix B.

2.3.2. Non-uniform finite volume discretization with additional nodes (NUFVD+A)

One way of handling discontinuities is to place additional nodes around all discontinuities, i.e. around texture edges [4,5,15]. The utilized

methodology is outlined in the following only for the east side of a certain CV, as the procedure is equivalent for the other sides. During the mesh generation coordinates of all discontinuous CV boundaries are stored. Subsequently, the circumferential size of both adjacent CVs is evaluated. Additional CVs are then placed on both sides of the discontinuity, having a circumferential size of

$$\Delta\theta_{CV} = d_f \cdot MIN\left(\Delta\theta_{i,j}, \Delta\theta_{i,j+1}\right) \tag{15}$$

where i and j are the positions of the CV in radial and circumferential direction respectively, and d_f is the *discontinuity coefficient* (see Fig. 4). Using a very small value for the discontinuity coefficient can result in instability whereas a very big value will not result in notable discretization error improvements. Test simulations have shown that good results are achieved with $d_f = 0.1$ and therefore this value is used in this study.

2.3.3. Modified non-uniform finite volume discretization (MNUFVD)

The sudden variation in film thickness results in a sudden variation in pressure and consequently the pressure distribution becomes discontinuous itself. This is often referred to as *concentrated inertia effect* and can be considered by setting up a generalized Bernoulli equation just before and after the jump in film thickness:

$$p^- + \frac{\rho u^{-2}}{2} = p^+ + \frac{\rho u^{+2}}{2} + \xi \frac{\rho[MAX(u^-, u^+)]^2}{2} \tag{16}$$

where "−" denotes the location just before the jump (upstream) and "+" the location just after the jump (downstream). p and u denote the local pressure and average fluid velocity at these locations and ξ is an additional correction factor or *pressure drop coefficient*.

A way to incorporate this effect in a general finite volume discretization was proposed by Arghir et al. [6] and subsequently used to analyse textured slider bearings by Dobrica and Fillon [16]. In Ref. [16] it was also shown that the application of this method extends the validity of the Reynolds equation for flows with higher Reynolds numbers or deeper textures. Thus, implementing this method allows the application of Reynolds-based models for most configurations, avoiding the more time-consuming solution of the full Navier-Stokes system of equations. This method is adapted in the following for the present non-uniform, polar system in two dimensions. Note that the MNUFVD method in its present form is limited to the pressurised regions of the solution domain ($\mathscr{D}^+$), where the Reynolds equation is elliptic. For this reason, this method is only used if cavitation does not occur. The approach is presented only for the west cell boundary, as the procedure is equivalent for
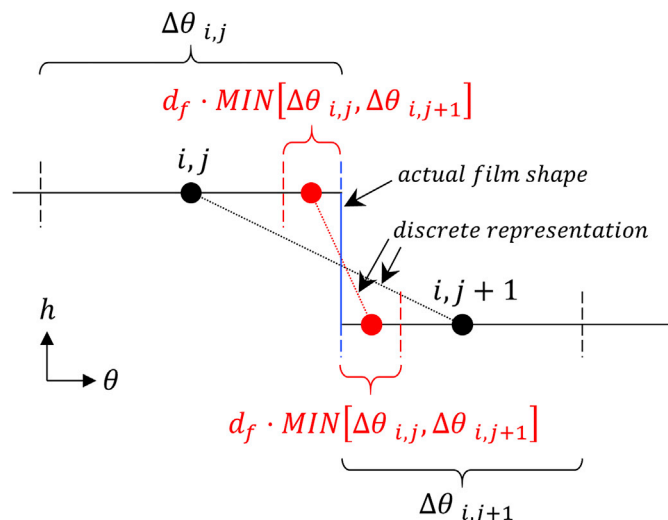
the other boundaries.

Without the presence of a discontinuity, values for film thickness and pressure at the west boundary of a certain CV are identical with the values at the east cell boundary of the CV just upstream, i.e. $h_{i,j}^w = h_{i,j-1}^e$ and $p_{i,j}^w = p_{i,j-1}^e$. As described in Ref. [6], this no longer holds true if the west cell boundary is discontinuous, hence $h_{i,j}^w \neq h_{i,j-1}^e$ and $p_{i,j}^w \neq p_{i,j-1}^e$. However, the interface flux continuity must still be respected, i.e. $q_{i,j}^w$ must equal $q_{i,j-1}^e$. Using additional interface values for film thickness and pressure at the cell boundaries, the aforementioned flow rate expression can be written as:

$$-\frac{A_{i,j}^w}{r_{i,j}^w}\Gamma_{i,j}^w\frac{p_{i,j}^P - p_{i,j}^w}{\delta\theta_{wP_{i,j}}} + 6\omega A_{i,j}^w r_{i,j}^w \rho_{i,j}^w h_{i,j}^w = -\frac{A_{i,j-1}^e}{r_{i,j-1}^e}\Gamma_{i,j-1}^e\frac{p_{i,j-1}^e - p_{i,j-1}^P}{\delta\theta_{eP_{i,j-1}}}$$
$$+ 6\omega A_{i,j-1}^e r_{i,j-1}^e \rho_{i,j-1}^e h_{i,j-1}^e \tag{17}$$

Rearranging and introducing the coefficients $b_{i,j}^w$ and $b_{i,j-1}^e$, one obtains:

$$b_{i,j}^w p_{i,j}^w + b_{i,j-1}^e p_{i,j-1}^e = b_{i,j}^w p_{i,j}^P + b_{i,j-1}^e p_{i,j-1}^P + 6\omega A_{i,j-1}^e r_{i,j-1}^e \rho_{i,j-1}^e h_{i,j-1}^e$$
$$- 6\omega A_{i,j}^w r_{i,j}^w \rho_{i,j}^w h_{i,j}^w \tag{18}$$

The required expressions for the interface pressures $p_{i,j}^w$ and $p_{i,j-1}^e$ are obtained from the generalized Bernoulli equation (eq. (16)):

$$p_{i,j}^w = p_{i,j-1}^e + B_w \tag{19}$$

where the *interface Bernoulli coefficient* for the west cell boundary is defined as:

$$B_w = -\frac{\rho\left(u_{i,j}^w\right)^2}{2} + \frac{\rho\left(u_{i,j-1}^e\right)^2}{2} - \xi\frac{\rho MAX\left[u_{i,j-1}^e, u_{i,j}^w\right]^2}{2} \tag{20}$$

The required average velocities are calculated from the corresponding flow rates:

$$u_{i,j}^w = \frac{q_{i,j}^w}{h_{i,j}^w} \quad and \quad u_{i,j-1}^e = \frac{q_{i,j-1}^e}{h_{i,j-1}^e} \tag{21}$$

Equations (18) and (19) now allow the evaluation of the interface pressure values as:

$$p_{i,j}^w = \frac{b_{i,j}^w}{b_{i,j}^w + b_{i,j-1}^e}p_{i,j}^P + \frac{b_{i,j-1}^e}{b_{i,j}^w + b_{i,j-1}^e}p_{i,j-1}^P + \frac{b_{i,j-1}^e}{b_{i,j}^w + b_{i,j-1}^e}B_w$$
$$+ \frac{6\omega A_{i,j-1}^e r_{i,j-1}^e \rho_{i,j-1}^e h_{i,j-1}^e}{b_{i,j}^w + b_{i,j-1}^e} - \frac{6\omega A_{i,j}^w r_{i,j}^w \rho_{i,j}^w h_{i,j}^w}{b_{i,j}^w + b_{i,j-1}^e} \tag{22}$$

$$p_{i,j-1}^e = \frac{b_{i,j}^w}{b_{i,j}^w + b_{i,j-1}^e}p_{i,j}^P + \frac{b_{i,j-1}^e}{b_{i,j}^w + b_{i,j-1}^e}p_{i,j-1}^P - \frac{b_{i,j}^w}{b_{i,j}^w + b_{i,j-1}^e}B_w$$
$$+ \frac{6\omega A_{i,j-1}^e r_{i,j-1}^e \rho_{i,j-1}^e h_{i,j-1}^e}{b_{i,j}^w + b_{i,j-1}^e} - \frac{6\omega A_{i,j}^w r_{i,j}^w \rho_{i,j}^w h_{i,j}^w}{b_{i,j}^w + b_{i,j-1}^e} \tag{23}$$

Repeating this procedure for the interface pressures at the east, south and north CV faces and substituting the obtained expressions in the general continuity equation allows to set up equations for the nodal values of pressure and fractional film content:

$$p_P = \frac{1}{a_P}\left(a_E p_E + a_W p_W + a_N p_N + a_S p_S + a_{\Theta W}\Theta_W + a_{\Theta P}\Theta_P + B_P + J_P\right) \tag{24}$$

and

$$\Theta_P = -\frac{1}{a_{\Theta P}}\left(a_E p_E + a_W p_W + a_N p_N + a_S p_S - a_P p_P + a_{\Theta W}\Theta_W + B_P + J_P\right) \tag{25}$$

Fig. 4. Schematic showing the placement of two additional control volumes around a discontinuity.

with the jump coefficient

$$J_P = \frac{6\omega A_{i,j-1}^e r_{i,j-1}^e \rho_{i,j-1}^e h_{i,j-1}^e b_{i,j}^w}{b_{i,j}^w + b_{i,j-1}^w} - \frac{6\omega A_{i,j+1}^w r_{i,j+1}^w \rho_{i,j+1}^w h_{i,j+1}^w b_{i,j}^e}{b_{i,j}^e + b_{i,j+1}^e} \tag{26}$$

and the Bernoulli coefficient

$$B_P = a_W B_w + a_E B_e + a_S B_s + a_N B_n \tag{27}$$

The remaining coefficients are given in Appendix C. Expressions (24) and (25) are similar to the expressions used for the NUFVD and NUFVD+A methods, however, two new parameters are present: B_P, which describes the effects of concentrated inertia at discontinuities through the generalized Bernoulli equation and J_P, which directly incorporates the jump in the film thickness distribution caused by texturing in the discrete equations.

Whenever the jumps in film thickness and pressure are neglected, the equations reduce to the ones found for the NUFVD and NUFVD+A method. If the jump term is included, film thickness discontinuities are incorporated and the first order pressure derivatives become discontinuous. In this case the problem remains linear, as the interface film thicknesses are already known. If both the jump in film thickness and pressure are considered, i.e. $J_P \neq 0$ and $B_P \neq 0$, both effects are incorporated in the solution and the pressure and its first order derivatives become discontinuous. In this case, an additional preceding loop is required to deal with the nonlinearity of the discrete system by updating the velocities based on the flow rates found in previous iterations. Formulating this set of equations for all internal nodes of the solution domain enables an iterative solution of the system.

2.4. Mesh generation

For untextured pads a uniform mesh is used, i.e. CVs are distributed evenly over the pad area. For textured pads, a uniform mesh is inefficient as only the complex textured portion of the pad requires a fine mesh. Hence, a non-uniform mesh is applied. The mesh generation is adaptive, i.e. CV edges are automatically aligned with the pad boundaries and texture edges. For improved computational performance, the present model allows to define different mesh densities for different pad areas: (i) The number of CVs inside each texture, (ii) The number of CVs in-between adjacent textures and (iii) The number of CVs for the untextured portions of the pad in circumferential and radial direction (see Fig. 5).

2.5. Numerical solution of the Reynolds equation

An iterative Gauss-Seidel method with successive relaxation is used to solve the discrete Reynolds equation. A mass-conserving cavitation algorithm similar to that proposed by Ausas [2] is applied, which correctly divides the solution domain into pressurized and cavitated areas and thus ensures an accurate prediction of film rupture and reformation boundaries. The following expressions are used for relaxation:

$$p_{i,j}^k = \omega_p \cdot p_{i,j}^k + (1 - \omega_p) \cdot p_{i,j}^{k-1} \tag{28}$$

$$\Theta_{i,j}^k = \omega_\Theta \cdot \Theta_{i,j}^k + (1 - \omega_\Theta) \cdot \Theta_{i,j}^{k-1} \tag{29}$$

where k denotes the iteration and ω_p and ω_Θ are the relaxation parameters for pressure and fractional film content respectively. Over-relaxation is used for pressure values and under-relaxation for fractional film content values. The convergence of the procedure is checked by the following criterion:

$$\varepsilon_p = \sum_{j=2}^{jj-1} \sum_{i=2}^{ii-1} \frac{|p_{i,j}^k - p_{i,j}^{k-1}|}{|p_{i,j}^k|} + \sum_{j=2}^{jj-1} \sum_{i=2}^{ii-1} \frac{|\Theta_{i,j}^k - \Theta_{i,j}^{k-1}|}{|\Theta_{i,j}^k|} \leq e_p \tag{30}$$

where ε_p is the sum of all nodal normalized fractional residuals of both pressure and film content and e_p is a predefined tolerance value (here $e_p = 10^{-5}$). No-slip boundary conditions are assumed at the fluid-solid interfaces and classic Dirichlet boundary conditions are imposed for pressures at all pad sides (here 10^4 Pa).

If the MNUFVD method is used and concentrated inertia effects are considered ($B_P \neq 0$), an additional preceding loop deals with the introduced nonlinearity of the discrete system. This loop calculates the average fluid velocities based on the flow rate results of the previous iteration and evaluates the required Bernoulli coefficients. To save computation time, this preceding loop is only performed for CVs actually having discontinuous boundaries. The solution of the Reynolds equation is performed directly in MATLAB whenever the discrete system is linear. If the system is nonlinear, the computation is performed in a sub-routine that runs in C as this was found to result in better performance.

2.6. Bearing equilibrium

The equilibrium is reached, if the pad angles and clearance define a film geometry that balances the applied load and causes no resultant moments around the pivot. This type of problem can be formulated as a nonlinear system:

$$\boldsymbol{F}(\alpha_r, \alpha_\theta, h_p) = \begin{bmatrix} \delta W(\alpha_r, \alpha_\theta, h_p) \\ \delta \theta(\alpha_r, \alpha_\theta, h_p) \\ \delta r(\alpha_r, \alpha_\theta, h_p) \end{bmatrix} = 0 \tag{31}$$

where δW is the difference between the load carrying capacity and the applied load, $\delta\theta$ and δr are the distances between the centre of pressure and the position of the pivot in circumferential and radial direction respectively. In the following, three different ways to solve this problem are discussed briefly. Detailed descriptions can be found in literature, e.g. Refs. [17,18]. As the numerical analysis of hydrodynamic bearings always involves the solution of a nonlinear problem similar to the one given in equation (31), the methods investigated below are also applicable for other types of textured or conventional bearings.

2.6.1. Newton-Raphson method

The Newton-Raphson method is one of the most popular techniques to solve nonlinear root-finding problems and has been used extensively in the study of hydrodynamic bearings. An initial approximation of the solution vector $\boldsymbol{x}^{k=1} = (\alpha_r^1, \alpha_\theta^1, h_p^1)^t$ is updated iteratively by the following expression:

$$\boldsymbol{x}^{k+1} = \boldsymbol{x}^k - \boldsymbol{J}(\boldsymbol{x}^k)^{-1} \boldsymbol{F}(\boldsymbol{x}^k) \tag{32}$$

where k denotes the number of the current iteration and $\boldsymbol{J}(\boldsymbol{x}^k)^{-1}$ is the inverse of the local Jacobian matrix at $\boldsymbol{x}^k$. The Jacobian matrix associated with point-pivoted pads takes the form:

$$\boldsymbol{J}(\boldsymbol{x}^k) = \begin{bmatrix} \dfrac{\partial \delta W}{\partial \alpha_r}(\boldsymbol{x}^k) & \dfrac{\partial \delta W}{\partial \alpha_\theta}(\boldsymbol{x}^k) & \dfrac{\partial \delta W}{\partial h_p}(\boldsymbol{x}^k) \\[2ex] \dfrac{\partial \delta \theta}{\partial \alpha_r}(\boldsymbol{x}^k) & \dfrac{\partial \delta \theta}{\partial \alpha_\theta}(\boldsymbol{x}^k) & \dfrac{\partial \delta \theta}{\partial h_p}(\boldsymbol{x}^k) \\[2ex] \dfrac{\partial \delta r}{\partial \alpha_r}(\boldsymbol{x}^k) & \dfrac{\partial \delta r}{\partial \alpha_\theta}(\boldsymbol{x}^k) & \dfrac{\partial \delta r}{\partial h_p}(\boldsymbol{x}^k) \end{bmatrix} \tag{33}$$

In the present work, finite difference formulae are utilized to calculate the partial derivatives of the Jacobian. Consequently, a single determination of the Jacobian matrix requires the complete evaluation of both pressure and film content distributions for four different film thickness distributions and a subsequent computation of load carrying capacity and centre of pressure. As the elements of the Jacobian are independent from each other, a simultaneous evaluation on multiple processor cores is possible and utilized in the present model.
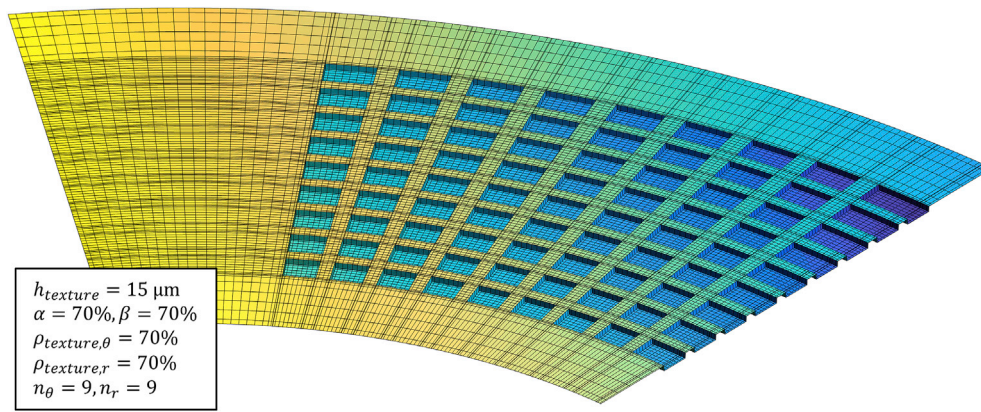
Fig. 5. Example mesh for a texture pattern with 9 × 9 textures: 7 × 7 CVs inside textures and 3 × 3 CVs in-between adjacent textures; 20 and 10 CVs for the untextured pad area in circumferential and radial direction respectively; Additional CVs placed around all discontinuities according to equation (15).

The Newton-Raphson iteration procedure stops when either convergence or a user-defined maximum number of iterations is reached. The convergence criterion used in this work is:

$$\varepsilon_e = \frac{|\delta W|}{W_0} + \frac{|\delta \theta|}{\theta_p} + \frac{|\delta r|}{r_p} \leq e_e \tag{34}$$

where the tolerance value for the equilibrium solver used here is 10^{-3} if not otherwise specified. Although the authors experienced a good convergence behaviour of Newton's method for most circumstances, a particularly poorly chosen initial guess for the film thickness distribution may, at times, lead to numerical instability. Therefore, an empirical numerical damping method is utilized, where the Jacobian is replaced by a *damped Jacobian*:

$$\boldsymbol{J}_{damped} = \left(\frac{D}{k^2} + 1 \right) \boldsymbol{J} \tag{35}$$

where D is the *damping parameter*. Several test simulations have shown that a damping parameter of $D = 1.5$ results in improved stability and computation time for most cases, therefore this value is used whenever damping is required, otherwise $D = 0$ and equation (35) reduces to the normal Jacobian matrix.

2.6.2. Broyden's method

The major drawback of Newton's method is the necessity to evaluate the Jacobian matrix at each iteration, resulting in high computation times. Broyden's method is a Quasi-Newton method that only requires the determination of the Jacobian matrix once. Although the convergence of this method is only superlinear as compared to the quadratic convergence of Newton's method, the computation effort during each iteration can be reduced significantly. The first improvement to an initial guess is obtained according to Newton's method, i.e. equation (32), requiring the determination of the Jacobian. For subsequent iterations new solutions are found with the following expression:

$$\boldsymbol{x}^{k+1} = \boldsymbol{x}^k - A_k^{-1} \boldsymbol{F}(\boldsymbol{x}^k) \tag{36}$$

The only difference to Newton's method is the use of the inverse of A_k instead of the inverse of the Jacobian matrix. A_k^{-1} is calculated based on a secant method and the matrix inversion formula of Sherman and Morrison [17]. The convergence criterion is the same as the one used for Newton's method. In the present model the initial guess is usually first updated by other algorithms or available results from previous calculations before starting the iteration with Broyden's method. If damping is required, the same damping procedure as introduced above for Newton's method is applied.

2.6.3. Continuation method

The aforementioned Newton-type methods generally require a fairly good approximation in order to converge. A possible remedy is a continuation or homotopy method [17,18], where the problem $\boldsymbol{F}(\boldsymbol{x}) = 0$ is transformed into a collection of problems parameterized by the homotopy parameter λ. Here, this is achieved by defending a convex homotopy $\boldsymbol{G}(\lambda, \boldsymbol{x})$, which allows the connection of the functions $\boldsymbol{G}(0, \boldsymbol{x})$ and $\boldsymbol{G}(1, \boldsymbol{x})$ as:

$$\boldsymbol{G}(\lambda, \boldsymbol{x}) = \boldsymbol{F}(\boldsymbol{x}) + (\lambda - 1) \boldsymbol{F}(\boldsymbol{x}(0)) \tag{37}$$

For $\lambda = 0$, equation (37) is a problem with known solution, corresponding to an initial film thickness guess $\boldsymbol{x}(0)$. For $\lambda = 1$, equation (37) is the original problem, corresponding to the film thickness encountered when the bearing is in equilibrium $\boldsymbol{x}(1)$. It is now possible to proceed from $\lambda = 0$ to $\lambda = 1$ in a finite number of steps by formulating $\boldsymbol{x}'(\lambda) = -\boldsymbol{J}(\boldsymbol{x}(\lambda))^{-1} \boldsymbol{F}(\boldsymbol{x}(0))$, which is a system of ordinary differential equations. The method used to solve this set of equations is the classic fourth-order Runge-Kutta method. Convergence is checked according to equation (34) after the procedure terminates.

2.7. Thermal effects

To approximate the temperature rise of the lubricant due to viscous shearing, an effective temperature method is applied [19], where the effective temperature is evaluated by:

$$T_{eff} = T_{inlet} + k_{con} \frac{\Pi}{Q_{in} \rho c_p} \tag{38}$$

where Π is the frictional power loss, Q_{in} is the pad inflow, c_p the lubricant specific heat and k_{con} the amount of heat removed by convection, typically $50\% \leq k_{con} \leq 100\%$ [20,21]. In the present study $k_{con} = 75\%$. T_{inlet} is the lubricant temperature at the pad inlet, which is calculated considering the hot-oil-carry-over-effect [22,23], where it is assumed that the oil entering a particular pad is a mixture of cold oil from the oil supply and hot oil transported over from the preceding pad:

$$T_{inlet} = \frac{T_{out} Q_{out} + T_{sup} Q_{sup} + T_{ir} Q_{ir}}{Q_{out} + Q_{sup} + Q_{ir}} \tag{39}$$

where T_{out} and Q_{out} are the temperature and mass flow rate at the preceding pad's outlet, T_{sup} and Q_{sup} the supply temperature and supplied mass flow rate and T_{ir} and Q_{ir} the temperature and mass flow rate leaving the preceding pad's inner radius.

The maximum pad temperature is approximated by the empirical relation [21]:

$$T_{max} = 2T_{eff} - T_{inlet} \tag{40}$$

The viscosity variation with temperature is modelled using the expression proposed by McCoull and Walther [21]:

$$\log_{10}[log_{10}(\nu_{cSt} + a)] = n - mlog_{10}(T_{\circ K}) \tag{41}$$

where ν_{cSt} is the lubricant kinematic viscosity in centistokes, $T_{\circ K}$ the temperature in degrees Kelvin and a, n and m are lubricant dependent parameters. In the present study, $a = 0.6$ and n, m are calculated based on the lubricant. The effective temperature, corresponding effective viscosity and inlet temperature are updated iteratively until thermal equilibrium is reached. The following convergence criterion is used for the temperature solver:

$$\varepsilon_t = \frac{\left|T_{eff}^{k+1} - T_{eff}^k\right|}{T_{eff}^{k+1}} \leq e_t \tag{42}$$

where e_t is a predefined tolerance value (here $e_t = 10^{-4}$). All intermediate results obtained during one temperature iteration (results of the equilibrium solver, different pressure and film content distributions) are generally stored and used as first approximations for the next temperature iteration to decrease computation time.

2.8. Overall numerical procedure

A simplified flow chart of the model is illustrated in Fig. 6 and explained briefly in the following.

After importing the input variables from a text file, the mesh is generated and the discrete system is prepared by applying the NUFVD,

NUFVD+A or MNUFVD method. The Reynolds equation is then solved using the Gauss-Seidel relaxation procedure until convergence is reached. Once pressure and fractional film content distributions are known, it is checked whether the bearing is in equilibrium and if not, pad angles and clearance are updated by the Newton-Raphson, Broyden or continuation method until the bearing is in equilibrium. Lastly, results are checked for thermal equilibrium and inlet temperature, effective temperature and corresponding effective viscosity are updated if required. Once all results are converged, the bearing performance parameters are evaluated. This procedure is either conducted for a bearing with untextured pads, textured pads or both. In the latter case results from the untextured bearing can be used as first approximations for the textured bearing to evaluate the impact of texturing on the bearing performance and decrease computation times as shown in the results section.

As the impact of texturing highly depends on the operating conditions, it is typically necessary to run multiple simulations for the range of operating conditions expected. Therefore, the present model allows to perform parametric studies by simply specifying load and speed steps in the input file. Moreover, parametric studies can also be performed for varying texture design parameters, such as texture depth or density to optimize texture patterns for a given application. To reduce computation time, parametric studies are performed simultaneously on multiple processor cores. Once all simulations are performed, results are stored in a combined *.csv file.

3. Numerical experiments

This section is devoted to comparing the aforementioned numerical methods in terms of computation speed and robustness. All scripts are
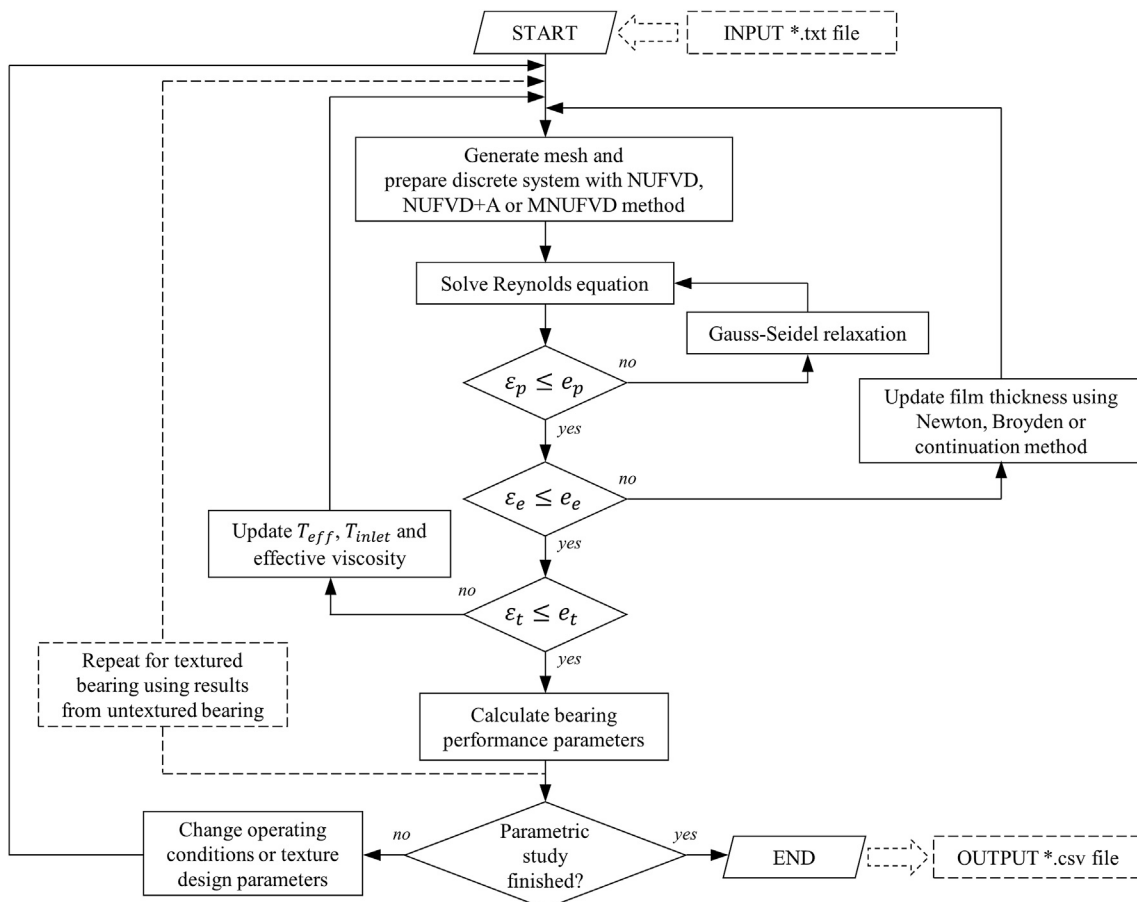

Fig. 6. Simplified flow chart of the numerical model.

written in MATLAB 2016b and simulations are performed on a desktop workstation with 16 GB RAM and *Intel Core i7-3770* @ 3.40 GHz CPU with four physical/eight logical cores. All numerical experiments are conducted on the point-pivoted tilting pad thrust bearing investigated in Refs. [22,23]. Geometrical details and considered operating conditions are given in Table 1.

For the purpose of this study, a relatively simple texture design with 5×5 textures is used to introduce discontinuities in the film thickness distribution in order to keep the computation times low and facilitate comparing the different numerical methods. However, conclusions will still hold true for more complex texture designs as higher numbers of textures only scale the size of the encountered discrete systems.

3.1. Comparison of discretization methods

To compare the three discretization methods in terms of computational speed and accuracy, a mesh study is conducted. The model is run for a given film thickness and effective temperature, i.e. only the fluid solver is utilized. The pre-defined film thickness and effective temperature are chosen to be approximately corresponding to a bearing operation at 1.0 MPa specific load. All input parameters are given in Table 2.

After running numerous simulations, it was found that the predicted load carrying capacity is the parameter most influenced by the mesh size. Therefore, this parameter is used for the mesh study. The procedure used to compare the discretization methods is similar to the one used by Woloszynski et al. [13] and is briefly explained in the following. The Reynolds equation is solved for an initial coarse mesh and subsequently the corresponding load carrying capacity is evaluated. This is done for the NUFVD, NUFVD+A and MNUFVD method successively. The MNUFVD method is used without the consideration of concentrated inertia effects at discontinuities, i.e. $B_P = 0$. The initial mesh consists of 2 CVs inside each texture, 1 CV in-between adjacent textures, 4 CVs for the untextured pad area in circumferential direction and 2 CVs each for the untextured pad areas in radial direction; or in short notation: 2/1/4/2. This corresponds to a mesh with a total of 20×20 CVs, hence $400°$ of freedom (DOF). The mesh is then iteratively refined using a global refinement factor of 1.25 and the calculations are repeated. This is done for a total of 17 meshes, resulting in a finest mesh with 458329 DOF (71/36/142/71). For every refinement, the consecutive error, i.e. the difference in predicted load carrying capacity between the current and previous mesh iteration, is evaluated. After all consecutive errors are known for all discretization methods and meshes, the predicted load carrying capacity of the method and mesh resulting in the smallest consecutive error is used as a reference value. This allows to evaluate the required DOF to reach a certain error with respect to the reference value for all three discretization methods and meshes.

Table 1
Bearing geometry and operating conditions considered.

Description	Symbol	Quantity
Bearing geometry		
Number of pads	n_{pad}	6
Inner pad radius (mm)	r_i	57.15
Outer pad radius (mm)	r_o	114.3
Pad angle (°)	θ_{pad}	50
Circumferential coordinate of pivot (°)	θ_p	30
Radial coordinate of pivot (mm)	r_p	85.725
Operating conditions		
Applied specific load (MPa)	w_0	0.5 … 2.0
Rotational speed (rpm)	ω	1500 and 3000
Lubricant		ISO VG 46
Density (kg/m³)	ρ	855
Viscosity at 40 °C (cSt)	ν_{40}	42.646
Viscosity at 100 °C (cSt)	ν_{100}	6.499
Supply oil flow rate (l/min)	Q_{sup}	15
Supply oil temperature (°C)	T_{sup}	50
Lubricant specific heat (J/kg/K)	c_p	2035

Table 2
Input parameters for the mesh study.

Description	Symbol	Quantity
Film thickness at pivot position (µm)	h_p	50
Pitch angle (µrad)	α_r	400
Roll angle (µrad)	α_θ	−185
Rotational speed (rpm)	ω	3000
Effective temperature (°C)	T_{eff}	70
Texture depth (µm)	$h_{texture}$	15
Texture extent in circumferential direction (%)	α	70
Texture extent in radial direction (%)	β	70
Texture density in circumferential direction (%)	ρ_θ	63.25
Texture density in radial direction (%)	ρ_r	63.25
Inlet textured?		yes

Fig. 7 shows the predicted load carrying capacity for the different meshes and discretization methods. Results are plotted over DOF rather than a mesh index as additional CVs are added when using the NUFVD+A method.

A clear trend towards a common load carrying capacity of approximately 3885 N can be observed for all methods. For all meshes studied, the MNUFVD method showed the smallest consecutive errors, followed by the NUFVD+A method. Largest errors were obtained with the NUFVD method. Therefore, the reference value is determined by the MNUFVD method at the finest mesh ($W_{ref} = 3884.95$ N). The relative differences to the reference value can now be evaluated for all methods and meshes (see Fig. 8).

It is evident that the MNUFVD exhibits superior performance, followed by the NUFVD+A method. Highest errors are obtained when using the NUFVD method. As the expected influence of surface texturing on the load carrying capacity usually lies in a single figure percent range, the DOF required to achieve errors of 1%, 0.5% and 0.1% are compared. Note however that the evaluated required DOF are approximations as the meshes are refined incrementally. The conventional NUFVD method requires 5700, 31862 and 458329 DOF to achieve errors of 1%, 0.5% and 0.1% respectively. If additional nodes are placed around discontinuities (NUFVD+A), these errors can be achieved with much coarser meshes. Only 3364, 4225 and 17956 DOF are required to achieve errors of 1%, 0.5% and 0.1% respectively, resulting in a considerably more efficient solution of the Reynolds equation. The lowest number of DOF is required by the MNUFVD method, where errors of 1%, 0.5% and 0.1% are achieved with 961, 1444 and 9120 DOF respectively.

The pressure distribution obtained with the NUFVD+A method for 17956 DOF is shown in Fig. 9 for example. For reference, the pressure distribution for the equivalent untextured pad is also plotted.

It is evident that the texture pattern has a significant influence on the pressure development and is clearly reflected in the pressure distribution. Although closer to the pad inlet pressures are partially below the equivalent untextured pad, the maximum pressure is considerably increased from 1.88 MPa to about 2.39 MPa at the last texture row's edge, resulting in a higher load carrying capacity and potentially superior bearing performance. Fig. 10 shows the pressure distribution at the pad's mean radius for the three discretization methods investigated. It can be seen that the NUFVD method highly overestimates the maximum pressure and load carrying capacity due to the inaccurate approximation of the film at discontinuities. Placing additional nodes around the discontinuity lines results in a better representation of the real geometry and provides pressure values very close to the ones obtained with the MNUFVD method where additional pressure and film thickness values are considered directly on discontinuity lines without increasing the required DOF.

To compare the discretization methods in terms of computational speed, the CPU time required to solve the Reynolds equation is also evaluated. Although the mesh preparation takes slightly longer for both the NUFVD+A and MNUFVD method, the influence is very small and therefore not considered. Hence, times required for the sole solution of
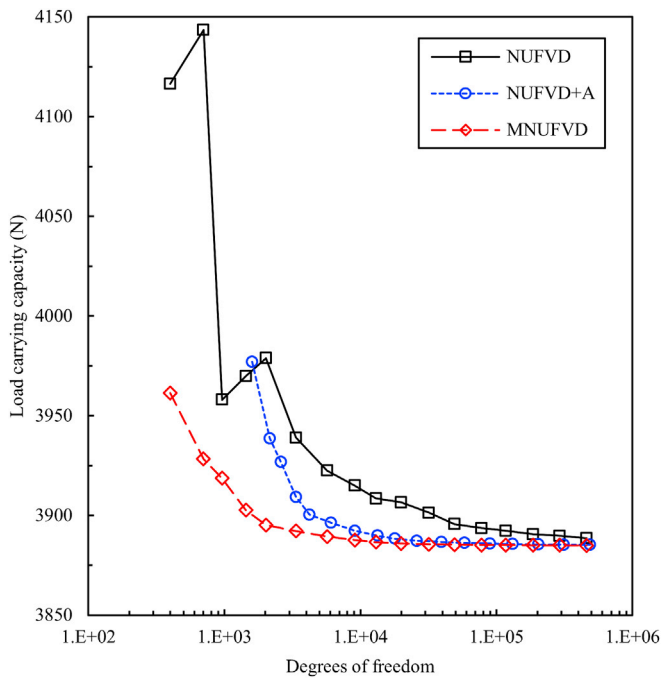
Fig. 7. Load carrying capacity as predicted by the different discretization methods for different meshes.
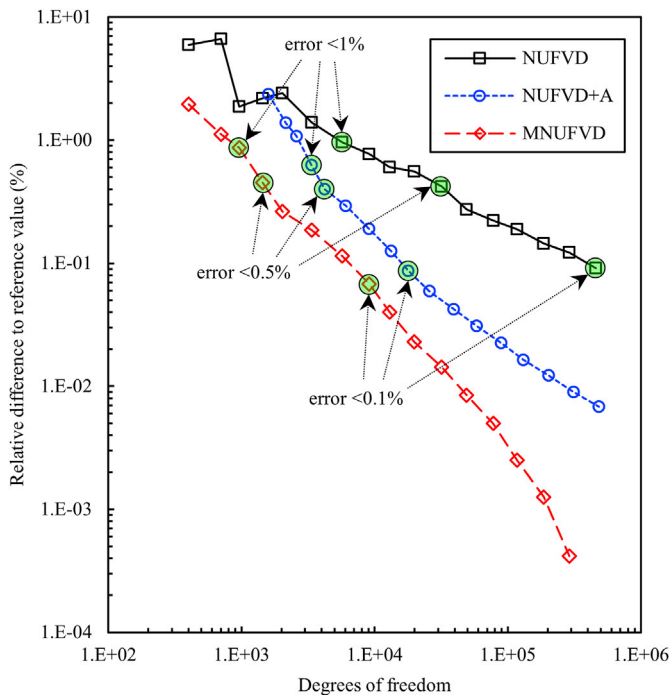

Fig. 8. Relative differences to the reference value for different discretization methods and meshes.

the Reynolds equation are compared. Note that encountered computation times are relatively low for all methods due to the simplicity of the analysed texture pattern. Therefore, the more complex implementation of the NUFVD+A and MNUFVD methods may not be justified for the present example. However, when simulating more complex texture patterns or conducting parametric/optimization studies the application of these methods becomes necessary. As the computation time significantly

depends on the relaxation parameter (ω_p) and the optimum relaxation parameter ($\omega_{p,opt}$) depends on the mesh details and discretization method used, simulations are performed with a fixed relaxation parameter of 1.98 as well as with the individually optimized relaxation parameter. The respective optimum relaxation parameters are iteratively found and optimized to three decimal places. Given computation times are arithmetic means of five consecutively run simulations.

As shown in Fig. 11, the conventional NUFVD method results in the highest computation times for all cases considered. Considerable improvements can be achieved by using the NUFVD+A method. For the case of non-optimized relaxation parameters, the computation is 1.7, 7.8 and 399 times faster as compared to the conventional NUFVD method to achieve errors of 1%, 0.5% and 0.1% respectively. When using optimized relaxation parameters, a speedup by a factor of 1.6, 12.3 and 137 is possible for errors of 1%, 0.5% and 0.1% respectively. Notably lowest computation times are encountered when the MNUFVD method is used. The CPU time needed to solve the Reynolds equation is 5.6, 22.6 and 767 times lower as compared to the NUFVD method when a fixed relaxation parameter is used. For optimized relaxation parameters speedup values change to 10, 63 and 431. For all cases considered realizable improvements increase with an increase in DOF.

For comparison, if concentrated inertia effects are considered in the MNUFVD method with $\xi = 0$ for the case of $\omega_p = \omega_{p,opt}$, computation times increase from 0.014, 0.024 and 0.264 to 0.388, 0.641 and 4.495 s to reach errors of 1%, 0.5% and 0.1% respectively. These CPU times are required if the nonlinear discrete system is solved directly in MATLAB. Solving the same problem in C reduces those computation times to 0.031, 0.055 and 0.625 s, being about 1 order of magnitude faster. However, this is only the case whenever the discrete system is nonlinear.

In conclusion, significant improvements in discretization error and computational speed can be achieved by treating discontinuities with the NUFVD+A or MNUFVD method. If a non-uniform discretization is already available, a modification to allow a placement of additional nodes as required by the NUFVD+A method is rather simple. Although superior, the MNUFVD method is more complex to implement and is limited to problems without cavitation. However, as mentioned above, cavitation does not usually occur for textured tilting pad thrust bearings. In fact, cavitation did not occur for any of the simulations presented in this paper. If cavitation occurs for the majority of operating conditions (e.g. journal bearings or parallel slider bearings), the reader may be interested in the FBNS algorithm [24].

3.2. Comparison of solution strategies for the equilibrium solver

The three root-finding methods for nonlinear systems introduced above for solving the equilibrium problem are compared in terms of computational speed and numerical stability. For simplicity, the following abbreviations are used from here on forth: N: Newton-Raphson method/B: Broyden's method with Sherman-Morrison formula/C: continuation method with fourth-order Runge-Kutta technique. Also, combination of these methods are compared: C2(+B): continuation method with two steps and consecutive solution with Broyden's method in case convergence is not reached by the continuation method alone/ N3+B: Newton's method performed for three iterations and consecutive solution with Broyden's method.

Simulations are performed for the same bearing and texture design as above, operating at 3000 rpm and 1.0 MPa specific load. Discretization is performed using the MNUFVD method without considering concentrated inertia for 9120 DOF and the temperature is pre-defined and constant at $T_{eff} = 70\,^{\circ}\text{C}$.

3.2.1. Quality of initial guess unknown

Firstly, cases are considered where the quality of the film thickness guess is unknown, which corresponds to an initial user-defined guess. Hence, no previous knowledge of the film thickness is available. Simulations are run with the available root-finding methods for three different
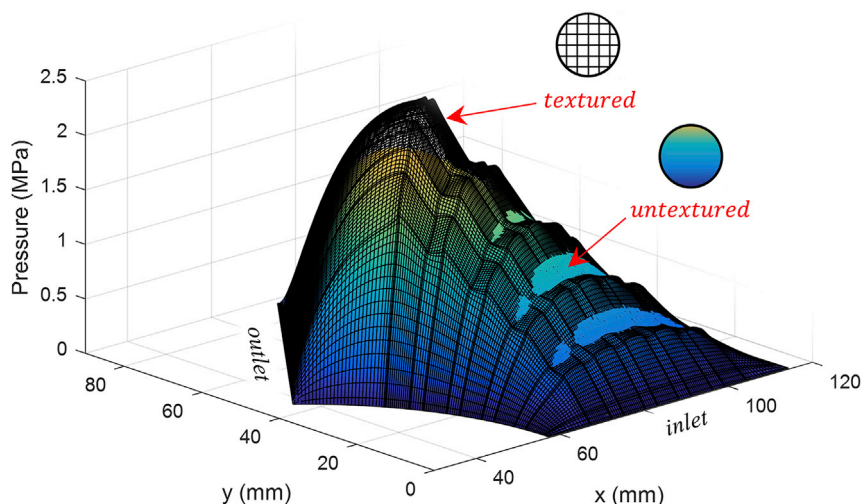
Fig. 9. Predicted pressure distribution for the textured pad with the NUFVD+A method and 17956 DOF and predicted pressure distribution for the equivalent untextured pad as obtained with a uniform mesh of 51 × 51 CVs (*.fig file available online).
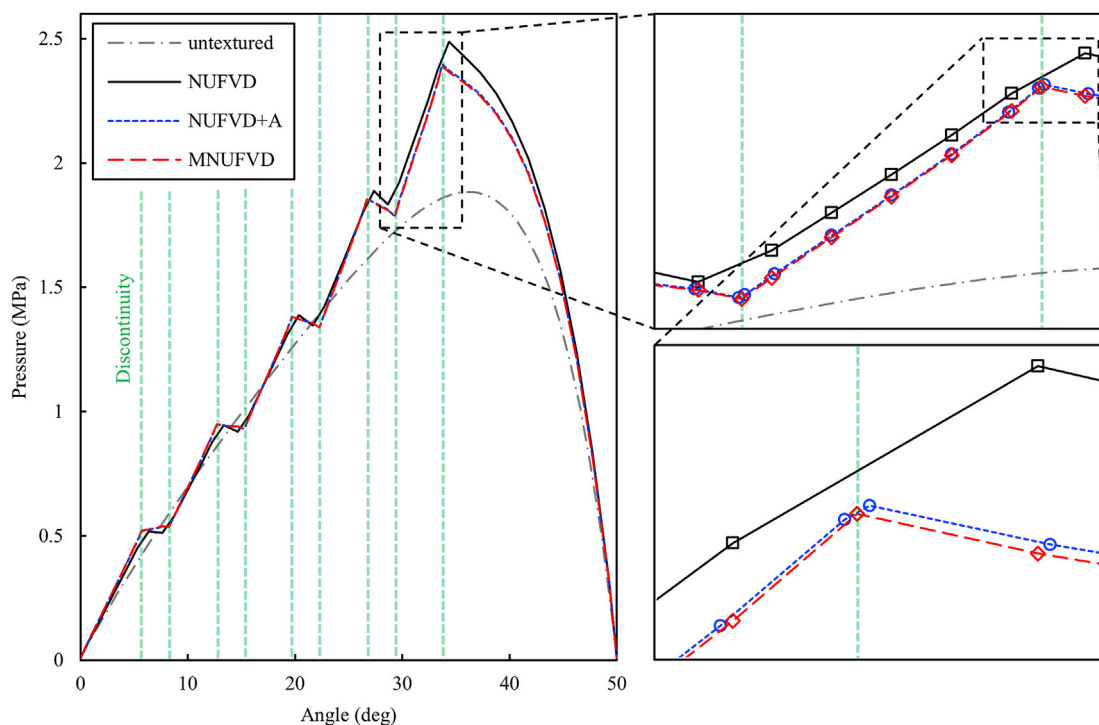

Fig. 10. Pressure distribution at the mean radius as predicted by different discretization methods for mesh 5: 5/2/10/5.

qualities of the initial guess: A good initial guess 10% away from the actual solution, an average guess 50% away from the solution and a poor guess 100% away from the solution. For comparison, all simulations are repeated for the case of one computational thread and four threads with and without damping. Total computation times to find the equilibrium are shown in Fig. 12 and more detailed in Table 3.

As seen in Fig. 12 (a), a particularly poorly chosen initial guess will not be sufficient for most methods to converge. The only method converging for this case is the C2(+B) method, requiring three additional Broyden iterations to converge, resulting in a total CPU time of 11.8 s. Note that this requires a total of 38 solutions of the Reynolds equation: 32 times for the four required computations of the Jacobian matrix for each step of the continuation method, four times for the Jacobian matrix required for the first Broyden iteration and two more times for iterations two and three of Broyden's method. For the guess of average quality, all

but the N1+B method converge. In this case the fastest methods are the N, C1(+B) and N4+B method with computation times ranging from 6.4 s for the C1(+B) method to 6.9 s for the N method. If the guess is close enough to the actual solution, all methods run stable and provide converged solutions. This time the conventional Newton method is fastest, requiring only three iterations, i.e. a total of 12 solutions of the Reynolds equation and resulting in a CPU time of 3.1 s. It is evident that the parallelization of the determination of the Jacobian matrix improves Newton's method enough to overshadow the advantage of Broyden's method. Broyden's method converges on its own, requiring 5 iterations, i.e. only 8 solutions of the Reynolds equation as compared to the 12 solutions Newton's method requires. The fact that Newton's method is faster anyway can be explained by the speedup achieved by multi-threading the evaluation of the Jacobian. For the MNUFVD method with 9120 DOF, the speedup factor by parallelization is approximately 2.7.
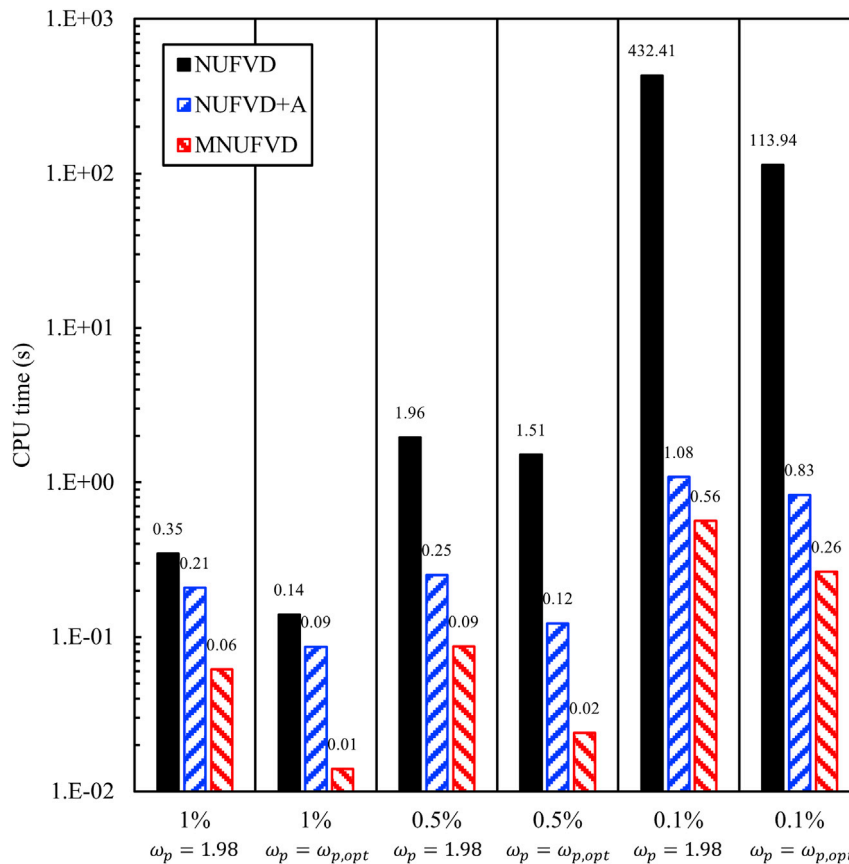
Fig. 11. CPU time required to solve the Reynolds equation for different discretization methods, desired errors and relaxation parameters.

This means that four solutions of the Reynolds equation take effectively only just about as long as 1.5 serial solutions of the Reynolds equation. Although the first iteration of Broyden's method also benefits from parallelization, Newton's method is slightly faster than Broyden's method nevertheless.

This is not the case when no multithreading is utilized (see Fig. 12 (b)). Here, the advantage of Broyden's method to only have to calculate the Jacobian once is more influential. This, for the case of a good quality guess, results in Broyden's method being the fastest with 5.7 s CPU time, being about 1.5 times as fast as the conventional Newton method. For the average guess, Broyden's method is fastest again, being approximately 1.4 times as fast as Newton's method. The slowest method is the C2(+B) method, which is 2.3 and 4.2 times slower than Broyden's method for the average and good guess respectively. For the poor guess, no comparison is possible as none of the methods except C2(+B) converge.

Results are different when the proposed damping procedure is applied (see Fig. 12 (c)). Now, for the case of a poor initial guess, all methods but C1(+B) converge. Fastest method is the conventional Newton-Raphson method, requiring six iterations and resulting in 6.75 s total computation time. Although Broyden's method usually demands a guess relatively close to the actual solution, the damping procedure results in a stable solution even for the poor initial guess. The computation time for this case is about twice as high as compared to the damped Newton method. For the average and good quality cases, the damped Newton method is fastest again. Longest computation times are generally encountered for the C2(+B) method and interestingly C1(+B) only converges for the good quality guess.

When damping is applied and the Jacobian is evaluated in series, Broyden's method is fastest for an average guess, being about 8% faster than Newton's method (see Fig. 12 (d)). For a good initial guess, N1+B is fastest with 9.4 s and for a poor initial guess N3+B with 15.9 s. Again,

highest computation times are required by the C2(+B) method, being as high as 33.8 s for the case of a poor quality guess. A point that is not discussed in detail is the fact that required iterations to solve the Reynolds equation depend on the film geometry as well. However, the influence is insignificant and is therefore not considered in the present comparison. For example, the required iterations to solve the Reynolds equation are 918, 918, 921 and 905 for the film geometry corresponding to the actual solution, the good quality guess, the average quality guess and the poor quality guess respectively.

In conclusion, the advantages of Broyden's method are generally overshadowed by the speedup achieved by parallelizing the evaluation of the Jacobian matrix. Therefore, a conventional Newton method is recommended whenever the quality of the first guess is unknown. If only one thread is available, the implementation of Broyden's can result in considerable improvements in terms of computation times, although damping may be required for poor quality guesses to improve stability. As an alternative to damping, a continuation method with at least two steps seems to provide improved numerical stability although CPU times are increased and the implementation is more complex.

3.2.2. Quality of initial guess known

As discussed above, Broyden's method performs best for initial guesses of good quality. One way to be capable of assessing the quality of the initial approximation of the film thickness distribution and therefore efficiently applying Broyden's method, is the use of results from a previous simulation of the equivalent untextured bearing. The idea behind this is to first run a complete bearing simulation for the equivalent untextured bearing and then use all obtained results as first approximations for the textured bearing. Although surface texturing alters the bearing equilibrium, changes are usually subtle. Hence, it can be assumed that results from the untextured bearing are good quality approximations
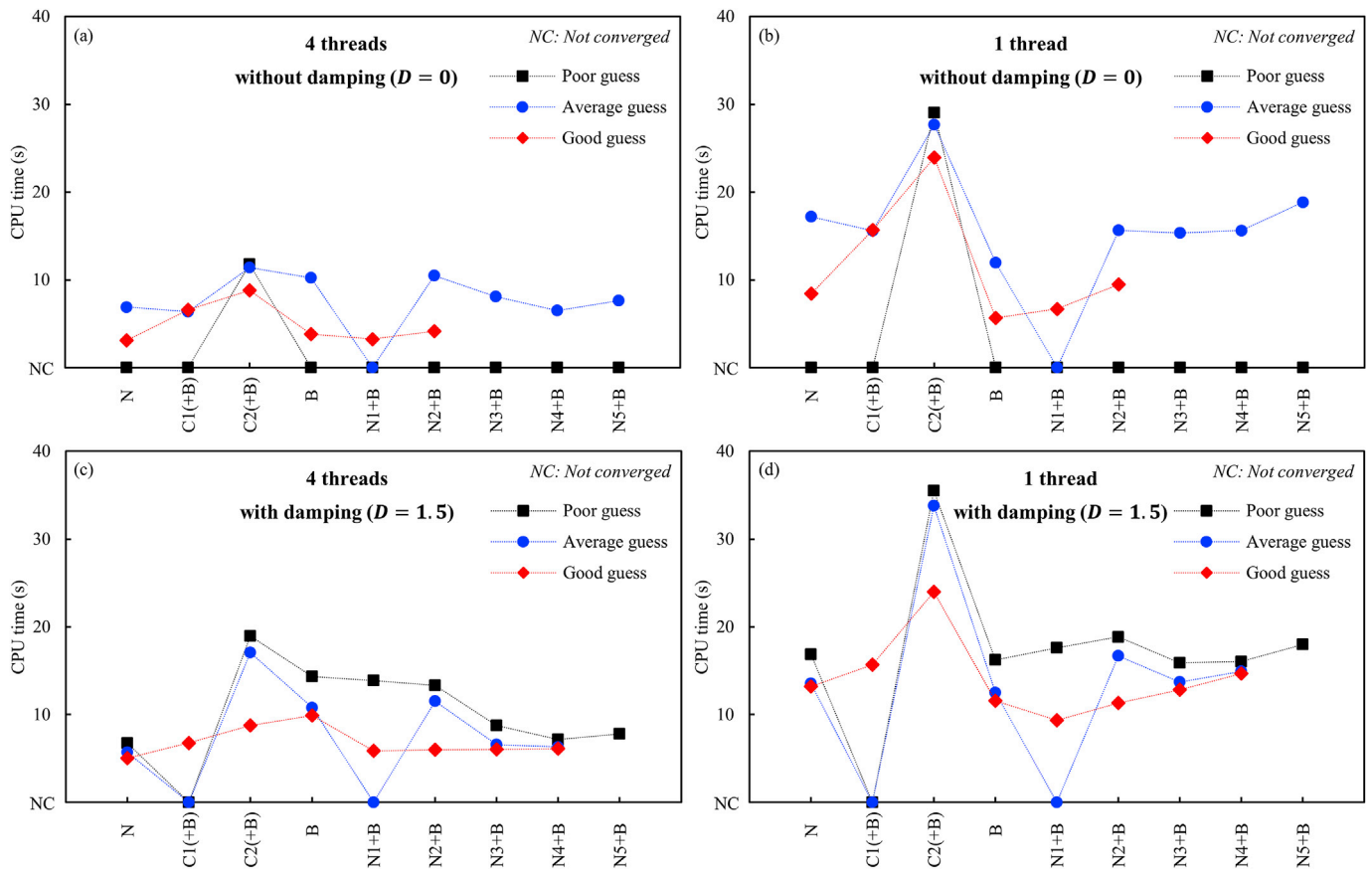
Fig. 12. Total simulation times for different equilibrium solver strategies: (a) 4 threads without damping, (b) 1 thread without damping, (c) 4 threads with damping and (d) 1 thread with damping.

for the textured bearing. The simulation of an untextured bearing is straightforward and can be done with relatively coarse and uniform meshes. Hence, only requiring a fraction of the time required to simulate a complexly textured bearing.

To analyse possible improvements by this methodology, simulations are run for the same conditions as above, using an average quality guess for the textured bearing as well as the untextured bearing. For the untextured bearing, a coarse uniform mesh with 11×11 CVs is used. Three methods are compared: Running only the simulation for the textured bearing with Newton's method (N), running the simulation first for the untextured bearing with Newton's method and subsequently for the textured bearing with Newton's method while using the results of the untextured bearing (UT+N) and running the simulation first for the untextured bearing with Newton's method and subsequently for the textured bearing with Broyden's method while using the results of the untextured bearing (UT+B). Computation times are given in Fig. 13 (a) and in more detail in Table 4.

When four threads are utilized, the simulation with Newton's method takes 6.4 s. By using the UT+N method, the total computation time can be reduced to 3.4 s if Newton's method is used for both the untextured bearing and the textured one. Six iterations and 0.5 s are needed for the untextured bearing and 2.9 s and three iterations for the textured one. The initial guess for the textured bearing in this case is the solution of the untextured bearing, here: $\alpha_r = 380\,\mu\text{rad}$, $\alpha_\theta = -173\,\mu\text{rad}$ and $h_p = 46\,\mu\text{m}$. For the textured bearing this corresponds to a guess of very good quality, being on average about 4% away from the actual solution. If the textured bearing is solved with Broyden's method only, the execution time further decreases to 2.9 s. In this case only three Broyden iterations are necessary. Hence, computation times can be decreased by factors of approximately 1.9 and 2.2 by the UT+N and UT+B methods respectively. If the simulations are run on one thread only, these factors

increase to about 2.1 and 3.7. The non-parallelized simulation of the untextured bearing takes 0.25 s, being faster than the parallelized computation due to the communication overhead, which is notable for the small scale problem having just 11×11 CVs. Once again, achievable improvements are higher for the non-parallelized simulations.

The quality of the film thickness guess can also be approximated during consecutive temperature iterations. New effective and inlet temperatures will change the equilibrium film thickness less and less with increasing temperature iterations. Hence, it can be assumed that the film thickness from a previous temperature iteration is a good quality guess for the next temperature iteration. To assess possible improvements, the complete model is now run including the temperature solver. An initial guess of 50 °C is used for both inlet temperature and effective temperature. Used initial guesses for the film thickness are 50% away from the corresponding actual solution. Results are presented in Fig. 13 (b) and Table 5.

If only Newton's method is applied, seven temperature iterations are required to reach thermal equilibrium. A total of 92 solutions of the Reynolds equation are necessary for this case and execution times are 22.9 and 61.2 s for four threads and one thread respectively. For the first temperature iteration, 6 N iterations are necessary to find the bearing equilibrium and for the remaining six temperature iterations 4, 4, 3, 2, 2 and 2 iterations. If Newton's method is only applied for the first temperature iteration and for all remaining iterations Broyden's method (NT1+B), computation times are reduced by factors of 1.03 and 1.4 to 22.2 and 42.5 s for four threads and one thread respectively. For these cases, the equilibrium position corresponding to the first temperature iteration is solved with 6 N iterations, the following six temperature iterations with 6, 6, 3, 2, 2 and 2 Broyden iterations, resulting in a total of 63 solutions of the Reynolds equation. If effective temperature, inlet temperature and equilibrium position are first found for the equivalent

Table 3
Total CPU time, required iterations and required solutions of the Reynolds equation (RE) for different equilibrium solver strategies.

Method		4 threads Poor guess (+100%) CPU time	Iterations[a]	RE solved	Average guess (+50%) CPU time	Iterations[a]	RE solved	Good guess (+10%) CPU time	Iterations[a]	RE solved	1 thread Poor guess (+100%) CPU time	Iterations[a]	RE solved	Average guess (+50%) CPU time	Iterations[a]	RE solved	Good guess (+10%) CPU time	Iterations[a]	RE solved
Without damping	N	NC	NC	NC	6.9	6	24	3.11	3	12	NC	NC	NC	17.18	6	24	8.44	3	12
	C1(+B)	NC	NC	NC	6.38	2	21	6.6	2	21	NC	NC	NC	15.61	2	21	15.68	2	21
	C2(+B)	11.78	3	38	11.42	2	37	8.79	0	32	29.06	3	38	27.69	2	37	23.95	0	32
	B	NC	NC	NC	10.22	14	17	3.81	5	8	NC	NC	NC	11.94	14	17	5.68	5	8
	N1+B	NC	NC	NC	NC	NC	NC	3.25	2	9	NC	NC	NC	NC	NC	NC	6.69	2	9
	N2+B	NC	NC	NC	10.47	11	22	4.16	2	13	NC	NC	NC	15.66	11	22	9.49	2	13
	N3+B	NC	NC	NC	8.08	6	21				NC	NC	NC	15.34	6	21			
	N4+B	NC	NC	NC	6.5	2	21				NC	NC	NC	15.62	2	21			
	N5+B	NC	NC	NC	7.62	2	25				NC	NC	NC	18.85	2	25			
With damping ($D = 1.5$)	N	6.75	6	24	5.71	5	20	5.05	5	20	16.88	6	24	13.55	5	20	13.22	5	20
	C1(+B)	NC	NC	NC	NC	NC	NC	6.77	2	21	NC	NC	NC	NC	NC	NC	15.7	2	21
	C2(+B)	18.98	14	49	17.09	11	46	8.76	0	32	35.53	14	49	33.8	11	46	24	0	32
	B	14.33	20	23	10.8	15	18	9.92	14	17	16.22	20	23	12.52	15	18	11.59	14	17
	N1+B	13.89	19	26	NC	NC	NC	5.88	6	13	17.62	19	26	NC	NC	NC	9.35	6	13
	N2+B	13.33	16	27	11.55	13	24	5.99	5	16	18.85	16	27	16.69	13	24	11.34	5	16
	N3+B	8.77	7	22	6.58	4	19	6.04	3	18	15.89	7	22	13.7	4	19	12.85	3	18
	N4+B	7.18	3	22	6.31	2	21	6.11	2	21	16.04	3	22	14.93	2	21	14.68	2	21
	N5+B	7.81	2	25							18	2	25						

[a] For method N Newton iterations and for all other methods Broyden iterations.

untextured bearing, then used as first approximations for the textured bearing and all equilibrium positions of the textured bearing are found with Broyden's method only (UT+B), computation times reduce further to 9 and 14.4 s for four threads and one thread respectively, resulting in a speedup by factors of 2.6 and 4.3 as compared to the conventional approach. The simulation of the equivalent untextured bearing with 11 × 11 CVs requires seven temperature iterations to find thermal equilibrium, where only Newton's method is applied. Computation times for the untextured bearing are 0.8 and 1.7 s for one thread and four respectively. Again, due to the communication time required, the computation is faster if only one thread is utilized. The improved guesses for inlet and effective temperature lower the required temperature iterations for the textured bearing from seven to four. 3, 2, 2 and 2 Broyden iterations are required for the UT+B method, resulting in a total of 21 solutions of the Reynolds equation.

Using results from the equivalent untextured bearing may be interpreted as a special kind of multigrid method with the difference that textures are ignored and a coarse uniform mesh is used for the initial simulation. These results are then used as initial approximations for the textured case, where a fine, non-uniform mesh is used. The method is capable of reducing computation times for textured bearings significantly, especially when strategically combined with Broyden's method. Although introduced here for tilting pad bearings, this method is readily adaptable for other kinds of textured contacts under hydrodynamic conditions.

4. Comparison with CFD results

To assess the accuracy of the present model, simulations are performed for the tilting pad thrust bearing investigated through CFD by Zouzoulas and Papadopoulos [23]. Results are compared for the bearing performance characteristics considered most important, namely minimum film thickness, friction torque per pad, maximum temperature and maximum pressure. To evaluate the accuracy over a wide range of conditions, results are compared for eight different operating conditions (0.5, 1, 1.5 and 2.0 MPa at 1500 and 3000 rpm) and three different pad designs (untextured, pocket and circumferential grooves).

All simulations are run with a universal initial film thickness guess of $\alpha_r = 300$ µrad, $\alpha_\theta = -150$ µrad and $h_p = 35$ µm to also assess the stability of the present model. The initial guess for effective and inlet temperature is 50 °C, and tolerance values of $e_p = 10^{-5}$, $e_e = 10^{-2}$ and $e_t = 10^{-4}$ are used. Note that the quality of these guesses significantly depends on the operating conditions. A total of three simulations are run, i.e. one simulation per pad design, where the eight operating conditions are evaluated simultaneously on eight computational threads. For the untextured pad, a uniform mesh with 101 × 101 CVs is used and exclusively Newton's method is applied for the first temperature iteration followed by Broyden's method for the remaining temperature iterations. For the pocketed pad, the simulation is first run for the equivalent untextured pad with 11 × 11 CVs and then Newton's method is applied for the first temperature iteration and Broyden's method for the remaining temperature iterations. The mesh for the pocketed pad consists of a total of 109 × 89 CVs. To simulate the grooved pad, again the equivalent untextured solution as obtained with 11 × 11 CVs is used, however, the textured pad is then simulated by applying a continuation method with two steps for the first temperature iteration, followed by Broyden's method for the remaining temperature iterations. This is done because numerical instability is encountered when using Newton's method only, due to the fluctuations in the quality of the initial guess. The mesh for the grooved pad consists of 109 × 98 CVs. The MNUFVD method is used for the both the pocketed and grooved pad. The relaxation parameter for pressure is set to 1.93 and 1.98 for the untextured pad and textured pads respectively. Results of the validation study are shown in Fig. 14 in terms of the relative differences.

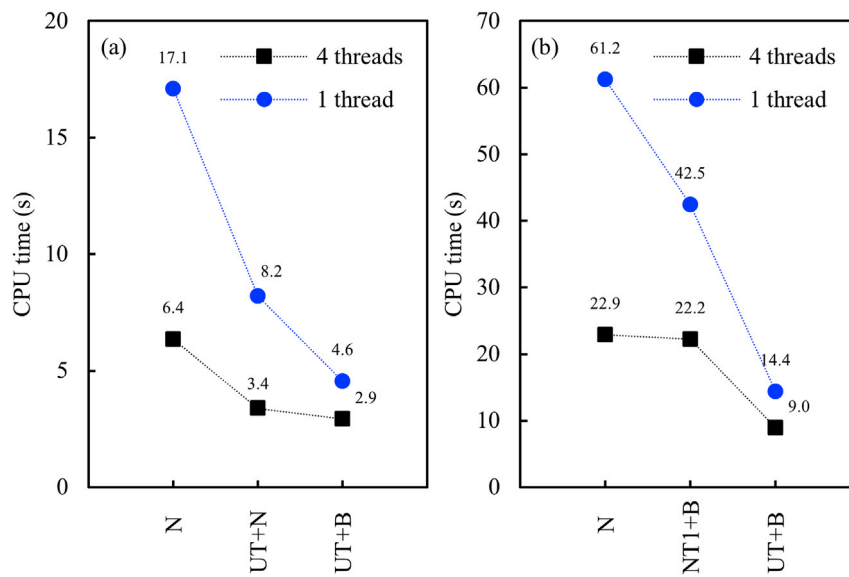Despite the use of a uniform initial guess, all performed simulations

Fig. 13. Total CPU time for different equilibrium solver strategies for two cases: (a) temperature is pre-defined and (b) temperature is found with the iterative temperature solver.

Table 4
Total CPU time and required iterations for different equilibrium solver strategies for a pre-defined temperature.

Method	4 threads			1 thread		
	CPU time	Iterations[a]	RE solved	CPU time	Iterations[a]	RE solved
N	6.36	6	24	17.09	6	24
UT+N	3.39	3	12	8.21	3	12
UT+B	2.93	3	6	4.56	3	6

[a] For method N and UT+N Newton iterations, for method UT+B Broyden iterations.

Table 5
Total CPU time and required iterations for different equilibrium solver strategies when applying the iterative temperature solver.

Method	4 threads			1 thread		
	CPU time	Iterations[a]	RE solved	CPU time	Iterations[a]	RE solved
N	22.9	6/4/4/3/ 2/2/2	92	61.2	6/4/4/3/ 2/2/2	92
NT1+B	22.2	-/6/6/3/2/ 2/2	63	42.5	-/6/6/3/2/ 2/2	63
UT+B	9.0	3/2/2/2	21	14.4	3/2/2/2	21

[a] For method N Newton iterations, for methods NT1+B and UT+B Broyden iterations.

converged, demonstrating the stability of the present model. The computation times were 55.2, 115.5 and 193.8 s for the untextured, pocketed and grooved pad respectively. It is evident that the obtained results for maximum pressure and friction torque by both models are remarkably similar, showing a maximum difference of just 3.3%. Generally, maximum pressure values are slightly overestimated by the present model, whereas predicted friction torque values are underestimated for the pocket design and evenly spread between −1.7% and 2.4% for the other two designs. Hence, obtained differences for p_{max} and T_f are relatively independent of the operating conditions. Larger differences are encountered for the predicted minimum film thickness and maximum temperature. Minimum film thickness values are underestimated for most cases, being slightly overestimated only for the untextured and grooved pad operating at 0.5 MPa and 3000 rpm. The largest difference for h_{min} is encountered for the untextured pad, being about −8.9% for an operation at 2.0 MPa and 1500 rpm. The differences in T_{max} show the most significant dependence on the operating

conditions, ranging from −10.5% to 10.9% for the untextured pad. For the pocketed and grooved pad differences in T_{max} range from −5.7% to 3.5%.

It is noteworthy that temperatures are generally overestimated for an operation at 1500 rpm and underestimated for an operation at 3000 rpm. This is due to the application of a constant convection parameter ($k_{con} = 75\%$), which overestimates convection at 1500 rpm and underestimates convection at 3000 rpm. It is evident that differences are more scattered for the untextured pad. This is related to the effective temperature method where a constant temperature is assumed over the entire pad area. This causes an underestimation of the tilt angles as local temperatures closer to the pad outlet are underestimated and local temperatures closer to the pad inlet overestimated. The higher the difference between inlet and outlet temperature, the higher the error in the predicted tilt angles. As these temperature differences are considerably smaller and less dependent on the operating condition for the pocketed and grooved pad, encountered differences between the present model and CFD are smaller and less scattered. In fact, it is likely that most differences are caused by the application of a simplified effective temperature method rather than solving the energy and heat conduction equations. However, in particular the results for friction torque and maximum pressure are remarkably close to the much more time consuming CFD simulation. In fact, the CFD simulation took approximately 64 h for each pad design according to the authors [23]. Hence, the present model is roughly three orders of magnitude faster than a comparable CFD study. Averaging the absolute values of all obtained differences into a single value yields 3%, which the authors deem sufficient for the purpose of texture design, especially considering the significant improvement in computational speed, which allows the numerical optimization of texture designs.

It should be noted that elastic deformation, the influence of surface roughness and turbulence effects were neglected in the present model and the CFD study. If more realistic results are required, the aforementioned effects should be considered.

5. Conclusions

This paper presents a numerical model to analyse textured tilting pad thrust bearings under hydrodynamic conditions. The Reynolds equation with mass-conserving cavitation is applied and thermal effects are considered using an effective temperature method. To improve accuracy and computational speed, three discretization methods are compared: a
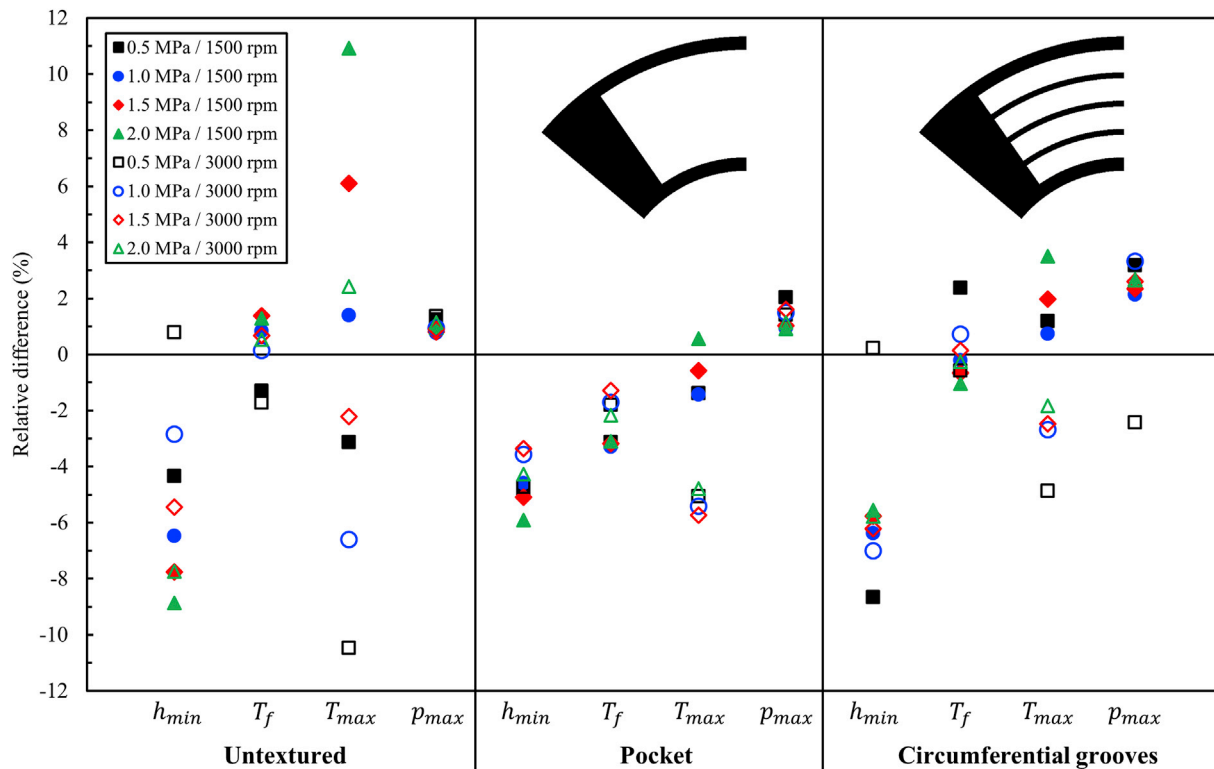
Fig. 14. Comparison of the results as predicted by the present model and CFD data from Ref. [23] for different pad designs and operating conditions.

non-uniform finite volume discretization (NUFVD), a version of this method where additional nodes are placed around discontinuities (NUFVD+A) and a modification to this method where discontinuities are directly incorporated in the discrete Reynolds equation (MNUFVD). Also, possible performance improvements by taking advantage of multiple processor cores are analysed and three equilibrium solvers (Newton-Raphson, Broyden's method and continuation with fourth-order Runge-Kutta) and combinations of those are compared. The performance of the numerical tool is enhanced by using results from the equivalent untextured bearing and the accuracy of the model is validated by comparison with data from commercial CFD software reported in literature. The main conclusions are:

- A special treatment of discontinuities can substantially decrease the computation time required to solve the Reynolds equation by retarding discretization errors, where the MNUFVD method results in higher performance improvements than the NUFVD+A method. In general, the lower the desired discretization error and hence, the finer the mesh, the higher the achievable speedup by the NUFVD+A and MNUFVD methods.
- Utilizing Broyden's method instead of Newton's method can be highly beneficial whenever the initial guess for the bearing equilibrium is sufficiently close to the actual solution. However, a parallel evaluation of the Jacobian matrix overshows this advantage in most cases. The algorithm with the best convergence behaviour is the continuation method with two steps. Newton's algorithm converges for most

scenarios and is comparably fast. The proposed damping procedure highly improves Newton's and Broyden's method in terms of numerical stability.
- Improving the initial film thickness guess by using results from the equivalent untextured bearing significantly reduces required CPU times, regardless of the equilibrium solvers utilized. In fact, the simulation of the untextured bearing and subsequent simulation of the textured bearing is much faster than the sole simulation of the textured bearing.
- The model is successfully validated by comparison with CFD data, where differences are smallest for predicted friction torque and maximum pressure values and highest for minimum film thickness and maximum temperature values. For the three texture configurations analysed, average errors are 5.3, 1.4, 3.6 and 1.7% for h_{min}, T_f, T_{max} and p_{max} respectively, while the present model is approximately three orders of magnitude faster than the CFD simulation.

Acknowledgements

Appendix A. Supplementary data

Supplementary data related to this article can be found at https://doi.org/10.1016/j.triboint.2017.10.024.

Appendix B. List of coefficients for NUFVD and NUFVD+A methods

$$a_W = \frac{A_w \Gamma_w}{r_w \delta\theta_{PW}} \tag{B.1}$$

$$a_E = \frac{A_e \Gamma_e}{r_e \delta\theta_{PE}} \tag{B.2}$$

$$a_S = \frac{A_s \Gamma_s r_s}{\delta r_{PS}} \tag{B.3}$$

$$a_N = \frac{A_n \Gamma_n r_n}{\delta r_{PN}} \tag{B.4}$$

$$a_P = a_W + a_E + a_S + a_N \tag{B.5}$$

$$a_{\Theta W} = 6\omega A_w h_w \rho_w r_w \tag{B.6}$$

$$a_{\Theta P} = -6\omega A_e h_e \rho_e r_e \tag{B.7}$$

Appendix C. List of coefficients for MNUFVD method

$$a_W = \frac{b_{i,j}^w b_{i,j-1}^e}{b_{i,j}^w + b_{i,j-1}^e} \tag{C.1}$$

$$b_{i,j}^w = \frac{A_{i,j}^w \Gamma_{i,j}^w}{r_{i,j}^w \delta\theta_{wP_{i,j}}} \tag{C.2}$$

$$b_{i,j-1}^e = \frac{A_{i,j-1}^e \Gamma_{i,j-1}^e}{r_{i,j-1}^e \delta\theta_{eP_{i,j-1}}} \tag{C.3}$$

$$a_E = -\frac{b_{i,j}^e b_{i,j+1}^w}{b_{i,j}^e + b_{i,j+1}^w} \tag{C.4}$$

$$b_{i,j}^e = -\frac{A_{i,j}^e \Gamma_{i,j}^e}{r_{i,j}^e \delta\theta_{eP_{i,j}}} \tag{C.5}$$

$$b_{i,j+1}^w = -\frac{A_{i,j+1}^w \Gamma_{i,j+1}^w}{r_{i,j+1}^w \delta\theta_{wP_{i,j+1}}} \tag{C.6}$$

$$a_S = \frac{b_{i,j}^s b_{i-1,j}^n}{b_{i,j}^s + b_{i-1,j}^n} \tag{C.7}$$

$$b_{i,j}^s = \frac{A_{i,j}^s r_{i,j}^s \Gamma_{i,j}^s}{\delta r_{sP_{i,j}}} \tag{C.8}$$

$$b_{i-1,j}^n = \frac{A_{i-1,j}^n r_{i-1,j}^n \Gamma_{i-1,j}^n}{\delta r_{nP_{i-1,j}}} \tag{C.9}$$

$$a_N = -\frac{b_{i,j}^n b_{i+1,j}^s}{b_{i,j}^n + b_{i+1,j}^s} \tag{C.10}$$

$$b_{i,j}^n = -\frac{A_{i,j}^n r_{i,j}^n \Gamma_{i,j}^n}{\delta r_{nP_{i,j}}} \tag{C.11}$$

$$b_{i+1,j}^s = -\frac{A_{i+1,j}^s r_{i+1,j}^s \Gamma_{i+1,j}^s}{\delta r_{sP_{i+1,j}}} \tag{C.12}$$

$$a_P = a_W + a_E + a_S + a_N \tag{C.13}$$

$$a_{\Theta W} = \frac{6\omega A_{i,j}^w r_{i,j}^w \rho_{i,j}^w h_{i,j}^w b_{i,j-1}^e}{b_{i,j-1}^e + b_{i,j}^w} \tag{C.14}$$

$$a_{\Theta P} = -\frac{6\omega A_{i,j}^e r_{i,j}^e \rho_{i,j}^e h_{i,j}^e b_{i,j+1}^w}{b_{i,j}^e + b_{i,j+1}^w} \tag{C.15}$$

References

[1] Gropper D, Wang L, Harvey TJ. Hydrodynamic lubrication of textured surfaces: a review of modeling techniques and key findings. Tribol Int 2016;94:509–29.

[2] Ausas RF, Ragot P, Leiva J, Jai M, Bayada G, Buscaglia GC. The impact of the cavitation model in the analysis of microtextured lubricated journal bearings. J Tribol 2007;129:868–75.

[3] Qiu Y, Khonsari MM. On the prediction of cavitation in dimples using a mass-conservative algorithm. J Tribol 2009;131:11.

[4] Xiong S, Wang QJ. Steady-state hydrodynamic lubrication modeled with the payvar-salant mass conservation model. J Tribol 2012:134. 031703-.

[5] Dobrica MB, Fillon M. Reynolds' model suitability in simulating rayleigh step bearing thermohydrodynamic problems. Tribol Trans 2005;48:522–30.

[6] Arghir M, Alsayed A, Nicolas D. The finite volume solution of the Reynolds equation of lubrication with film discontinuities. Int J Mech Sci 2002;44:2119–32.

[7] Guzek A, Podsiadlo P, Stachowiak GW. Optimization of textured surface in 2D parallel bearings governed by the Reynolds equation including cavitation and temperature. Tribol Online 2013;8:7–21.

[8] Rahmani R, Mirzaee I, Shirvani A, Shirvani H. An analytical approach for analysis and optimisation of slider bearings with infinite width parallel textures. Tribol Int 2010;43:1551–65.

[9] Jakobsson B, Floberg L. The finite journal bearing, considering vaporization, vol. 190. Tran Chalmers University of Tech Gothenburg; 1957. p. 1–116.

[10] Olsson KO. Cavitation in dynamically loaded bearings. Tran Chalmers University of Tech Gothenburg; 1965. p. 308.

[11] Bartel D. Simulation von Tribosystemen. Wiesbaden: Vieweg+Teubner; 2010.

[12] Woloszynski T, Podsiadlo P, Stachowiak GW. Evaluation of discretisation and integration methods for the analysis of hydrodynamic bearings with and without surface texturing. Tribol Lett 2013;51:25–47.

[13] Woloszynski T, Podsiadlo P, Stachowiak GW. Evaluation of discretization and integration methods for the analysis of finite hydrodynamic bearings with surface texturing. Proc Institution Mech Eng Part J-Journal Eng Tribol 2015;229:465–77.

[14] Versteeg HK, Malalasekera W. An introduction to computational fluid dynamics: the finite volume method. Pearson Education Limited; 2007.

[15] Dobrica MB, Fillon M, Pascovici MD, Cicone T. Optimizing surface texture for hydrodynamic lubricated contacts using a mass-conserving numerical approach. J Eng Tribol 2010;224:737–50.

[16] Dobrica MB, Fillon M. About the validity of Reynolds equation and inertia effects in textured sliders of infinite width. Proc Institution Mech Eng Part J J Eng Tribol 2009;223:69–78.

[17] Burden RL, Faires JD. Numerical analysis: brooks/cole. Cengage Learning; 2011.

[18] Kincaid DR, Cheney EW. Numerical analysis: mathematics of scientific computing. American Mathematical Society; 2002.

[19] Stachowiak GW, Batchelor AW. Engineering tribology. fourth ed. Amsterdam; London: Elsevier/Butterworth-Heinemann; 2014.

[20] Stachowiak GW, Podsiadlo P. 3-D characterization, optimization, and classification of textured surfaces. Tribol Lett 2008;32:13–21.

[21] Frene J, Nicolas D, Degueurce B, Berthe D, Godet M. Hydrodynamic lubrication: bearings and thrust bearings. Elsevier Science; 1997.

[22] Glavatskih SB, Fillon M, Larsson R. The significance of oil thermal properties on the performance of a tilting-pad thrust bearing. J Tribol 2001;124:377–85.

[23] Zouzoulas V, Papadopoulos CI. 3-D thermohydrodynamic analysis of textured, grooved, pocketed and hydrophobic pivoted-pad thrust bearings. Tribol Int 2017;110:426–40.

[24] Woloszynski T, Podsiadlo P, Stachowiak GW. Efficient solution to the cavitation problem in hydrodynamic lubrication. Tribol Lett 2015;58:1–11.